



HAL
open science

Further insights into the mechanisms involved in the corrosion of 316L(N) austenitic steel in oxygenated liquid sodium at 550 °C

Matthieu Rivollier, J.-L. Courouau, Michel Tabarant, Cécile Blanc, François Jomard, Marie-Laurence Giorgi

► To cite this version:

Matthieu Rivollier, J.-L. Courouau, Michel Tabarant, Cécile Blanc, François Jomard, et al.. Further insights into the mechanisms involved in the corrosion of 316L(N) austenitic steel in oxygenated liquid sodium at 550 °C. *Corrosion Science*, 2020, 165, pp.108399. 10.1016/j.corsci.2019.108399. cea-02870210

HAL Id: cea-02870210

<https://cea.hal.science/cea-02870210>

Submitted on 16 Jun 2020

HAL is a multi-disciplinary open access archive for the deposit and dissemination of scientific research documents, whether they are published or not. The documents may come from teaching and research institutions in France or abroad, or from public or private research centers.

L'archive ouverte pluridisciplinaire **HAL**, est destinée au dépôt et à la diffusion de documents scientifiques de niveau recherche, publiés ou non, émanant des établissements d'enseignement et de recherche français ou étrangers, des laboratoires publics ou privés.

1 Post print

2 Rivollier, Matthieu, Jean-Louis Courouau, Michel Tabarant, Cécile Blanc, François Jomard, et Marie-
3 Laurence Giorgi. « Further Insights into the Mechanisms Involved in the Corrosion of 316L(N)
4 Austenitic Steel in Oxygenated Liquid Sodium at 550 °C ». *Corrosion Science* 165 (1 avril 2020):
5 108399. <https://doi.org/10.1016/j.corsci.2019.108399>.

6

7 **Further insights into the mechanisms involved in the corrosion of 316L(N) austenitic**
8 **steel in oxygenated liquid sodium at 550 °C**

9 **Matthieu Rivollier^{1,2}, Jean-Louis Courouau^{2,*}, Michel Tabarant³, Cécile Blanc³,**
10 **François Jomard⁴, Marie-Laurence Giorgi^{1,*}**

11 ¹CentraleSupélec, Université Paris-Saclay, Laboratoire de Génie des Procédés et Matériaux, 3 rue
12 Joliot-Curie, F-91192 Gif-sur-Yvette cedex, France

13 ²Den-Service de la Corrosion et du Comportement des matériaux dans leur Environnement
14 (SCCME), CEA, Université Paris-Saclay, F-91191, Gif-sur-Yvette, France

15 ³Den- Service d'Études Analytiques et de Réactivité des Surfaces (SEARS), CEA, Université Paris-
16 Saclay, F-91191, Gif-sur-Yvette, France

17 ⁴GEMAC, Université de Versailles-St. QY., Université Paris-Saclay, 55 avenue de Paris, F-78000,
18 Versailles, France

19 matthieu.rivollier@ mailo.com; jean-louis.courouau@cea.fr; michel.tabarant@cea.fr;
20 cecile.blanc@cea.fr; francois.jomard@uvsq.fr; marie-laurence.giorgi@centralesupelec.fr

21 * Corresponding authors

22 **Abstract**

23 316L(N) austenitic steel was corroded at 550 °C in liquid sodium containing ca. 200 $\mu\text{g g}^{-1}$ dissolved
24 oxygen from 242 h to 7704 h. NaCrO_2 is formed for all immersion times, O and Na from liquid metal
25 and Cr from steel. The oxidation front is located at the chromite / steel interface and in the steel grain
26 boundaries. M_6C carbides (M = Mo and Fe) are also formed, C from liquid sodium. NaCrO_2 is dissolved
27 until the saturation of liquid sodium in Cr is reached. The Cr solubility is higher than that of pure Cr due
28 to the presence of dissolved oxygen.

29

30 **Keywords**

31 A. Stainless steel;

32 C. High temperature corrosion; interfaces; oxidation;

33

34

35 **1. Introduction**

36 Liquid sodium was chosen as the reference heat transfer fluid for the 4th generation of French nuclear
37 reactors because of its neutron and thermal properties, its excellent flow properties (low viscosity and
38 low density) and its compatibility with structural materials at high temperatures [1]. The temperature of
39 the reactor structure ranges from 400 °C to at least 550 °C with a low dissolved oxygen content (< 10
40 µg g⁻¹) under normal operating conditions. Although corrosion phenomena have limited effects under
41 these operating conditions, they must be well identified and predicted to ensure the service lifetime of
42 reactor structures. Indeed, some components such as the reactor vessel cannot be replaced and determine
43 the overall service lifetime of the reactor unit. The nominal lifetime is 60 years [2]. Similar corrosion
44 phenomena are expected for the fuel cladding operating at higher temperatures (650 °C at least) or for
45 the receivers in concentrated solar power plants (700 °C) [3].

46 The reference material for structures in contact with liquid sodium is the low carbon nitrogen-enriched
47 austenitic steel of the grade 316L(N) (18Cr-12Ni-2Mo) [4]. Liquid sodium corrosion of austenitic steels
48 has been extensively studied but until now these studies have not been critically reviewed. That is why
49 we started our study with a state of the art on liquid sodium corrosion.

50 Liquid sodium corrosion of austenitic steels includes the following two phenomena: 1) dissolution of
51 alloying elements (section 1.1) and 2) chemical reactions with impurities, such as oxidation (section 1.2)
52 and carburisation [5,6].

53

54 **1.1. Dissolution of alloying elements**

55 The dissolution of alloying elements in liquid sodium has been extensively studied in sodium loop
56 systems made of austenitic steel [7-14]. In these systems, the dissolved oxygen content was maintained
57 at less than about 10 µg g⁻¹ through a continuous purification unit. The sodium loop is divided into the
58 high temperature section, heat exchanger units and low temperature section. Chemistry control was
59 achieved by bypassing a fraction of the main flowrate to heterogeneous crystallisation units maintained
60 at low temperature, near the melting point, known as cold traps. These units are capable of reducing the
61 hydrogen and oxygen content to levels down to their solubility limits at 110 °C, while maintaining the
62 amount of alloying elements dissolved from the structural components at a constant level [15]. As the

63 solubility of alloying elements increases with temperature, mass transfer can occur from the hot section
64 where dissolution takes place to the cold section where precipitation of corrosion products takes place,
65 including those activated under the neutron flux (Co-60, Mn-54) leading to component contamination
66 [16]. Usually, the specimen to be investigated for corrosion was placed at the inlet of the hot isothermal
67 section, or downstream, provided that a specific correction was applied to take into account the alloying
68 elements into liquid sodium that reduces the dissolution rate [10,11].

69 **1.1.1. Empirical dissolution laws (dissolved O < 10 µg g⁻¹)**

70 After the dissolution or reduction of the native oxides, leading to wetting, a first step of corrosion begins,
71 the initial corrosion. Since some alloying elements, such as nickel, have a higher solubility than others,
72 selective leaching occurs, depending on temperature, hydrodynamics and oxygen content, first removing
73 nickel and then chromium and manganese. The result is a surface layer depleted in austenite stabilisers.
74 Under certain conditions (e.g., high temperature, degree of depletion), a ferrite layer composed mainly
75 of iron (> 95 wt.%) of a few µm thick is observed [6,8-14,16]. Liquid metal penetrations within some
76 grain boundaries are also observed [11,14], as well as a depleted austenitic layer below. Corrosion
77 kinetics appear to be high at first and decrease over time to a constant steady-state corrosion rate [6],
78 reflecting the change from a power law to linear kinetics.

79 A total mass loss, Δm (in mg dm⁻²) after 1 year of corrosion (during the initial step) can be calculated
80 by the following empirical relation for this steel grade [16]:

$$81 \quad \Delta m = 7.8 \cdot V_{Na}^{0.435} \cdot w_{O,ppm}^{Na} \cdot \exp\left(-\frac{150.5}{\theta - 544}\right) \quad \text{Eq. (1.1)}$$

82 where V_{Na} is the sodium velocity (in m s⁻¹), $w_{O,ppm}^{Na}$ is the oxygen concentration of sodium (in µg g⁻¹)
83 and θ is the temperature (in °C). θ is between 544 and 720 °C. This mass loss is significant only above
84 544 °C. The mass loss amounts to 641 mg dm⁻² for 7.6 m s⁻¹, 600 °C and 5 µg g⁻¹ of oxygen. It
85 corresponds to a dissolution thickness of 8 µm, assuming that the dissolution is uniform and neglecting
86 the degraded surface layer composed of ferrite and depleted austenite, thus underestimating slightly the
87 actual corrosion affected thickness.

88 During steady-state corrosion, generally for an immersion time of more than several thousand hours
89 [16], the ferrite layer initially formed on stainless steels is homogeneously dissolved [6]. The thickness
90 or the mass loss are computed by two types of empirical models.

91 The first one takes into account the effect of oxygen concentration ($w_{O,ppm}^{Na}$, in $\mu\text{g g}^{-1}$) and temperature
92 (T in K), as proposed in Eq. 1.2 [9,13,17-21]:

$$93 \log R_c = A_c + 1.5 \cdot \log w_{O,ppm}^{Na} - \frac{Q_c}{\ln 10 \cdot RT} \quad \text{Eq. (1.2)}$$

94 where R_c is the corrosion rate (in $\mu\text{m year}^{-1}$), A_c is a constant equal to 3.85 according to Thorley and
95 Tyzack for a Na velocity of 7.6 m s^{-1} and an oxygen content between 5 and $200 \mu\text{g g}^{-1}$ [13] (these values
96 show some dispersions in the recent literature, probably due to some conversion errors), Q_c is an
97 activation energy (in $\text{J mol}^{-1} \text{K}^{-1}$, usually $Q_c = 75,000 \text{ J mol}^{-1} \text{K}^{-1}$) and R is the gas constant ($R = 8.314$
98 $\text{J mol}^{-1} \text{K}^{-1}$). For comparison, the thickness dissolved amounts to $2.6 \mu\text{m year}^{-1}$ (201 mg dm^{-2}) for 600
99 $^{\circ}\text{C}$ and $5 \mu\text{g g}^{-1}$ of oxygen.

100 The second type of model takes into account two different corrosion mechanisms: (i) dissolution
101 depending on temperature only and (ii) reactions with oxygen depending on oxygen concentration and
102 temperature [19]:

$$103 R_m = A_m \cdot \exp\left(-\frac{Q_{m_1}}{RT}\right) + B_m \cdot w_{O,ppm}^{Na} \cdot \exp\left(-\frac{Q_{m_2}}{RT}\right) \quad \text{Eq. (1.3)}$$

104 where R_m is the mass loss rate (in $\text{mg cm}^{-2} \text{year}^{-1}$), A_m and B_m are constants ($A_m = 1.2 \cdot 10^{11} \text{ mg cm}^{-2}$
105 year^{-1} , $B_m = 3.8 \cdot 10^2 \text{ mg cm}^{-2} \text{year}^{-1}$), Q_{m_1} and Q_{m_2} are activation energies ($Q_{m_1} = 203,000 \text{ J mol}^{-1} \text{K}^{-1}$
106 1 , $Q_{m_2} = 58,600 \text{ J mol}^{-1} \text{K}^{-1}$). Brissonneau [16] reports that the first term of Eq. 1.3 should be related to
107 the preferential dissolution of Ni while the second term should be related to generalized corrosion. For
108 comparison, the thickness of dissolved steel amounts to $0.85 \mu\text{m year}^{-1}$ (68 mg dm^{-2}) for $600 ^{\circ}\text{C}$ and 5
109 $\mu\text{g g}^{-1}$ of oxygen.

110 In conclusion, whatever the corrosion step (initial or steady-state) and the empirical model considered,
111 the assessments of corrosion remain in the same order of magnitude and dissolved oxygen appears to be
112 one of the most important parameters of corrosion kinetics, even if its influence on dissolution is far
113 from obvious.

114

115 **1.1.2. Oxygen effects on dissolution (dissolved O < 10 µg g⁻¹)**

116 As shown in Section 1.1.1, the initial and steady-state corrosion rates of alloys depend on dissolved
117 oxygen. In general, the higher the oxygen concentration, the higher the corrosion rate (Eqs. 1.1, 1.2 and
118 1.3), with even a change from uniform to intergranular attack [22]. This is why in all systems containing
119 liquid sodium, dissolved oxygen is kept as low as possible. In general, the proposed corrosion rate
120 depends on the oxygen concentration according to a n power law, where n is 2 for pure iron, 1 for pure
121 chromium and 0 for pure nickel [6,11-13]. Only pure nickel (which does not form stable oxygen
122 compounds in liquid sodium) exhibits an oxygen-independent corrosion rate.

123 The solubility of iron appears to increase with dissolved oxygen content, resulting in a dissolution rate
124 that increases as dissolved oxygen content increases [1,9,23,24]. No oxygen and iron compounds are
125 expected to be stable in liquid sodium containing less than 10 µg g⁻¹ of dissolved oxygen and at
126 temperatures less than or equal to 550 °C. However, a Na-Fe-O complex may be formed that would
127 explain the experimental observations [9]. A Na-Cr-O complex could also be formed [25], although
128 sodium chromite (NaCrO₂) is stable in this case, i.e. for a few µg g⁻¹ of oxygen at 550 °C [26].

129 Finally, it was deduced from the overall results presented in Section 1.1 that the global dissolution
130 kinetics is related only to the iron dissolution rate [8,9]. The potential influence of chromium dissolution
131 on the steady-state dissolution has been ruled out, either because of its low solubility relative to iron
132 solubility [23,24], or because of the fast sodium saturation in chromium due to the high ratio of sample
133 surface area to sodium volume [25].

134 **1.2. Oxidation in liquid sodium containing oxygen (dissolved O > 10 µg g⁻¹)**

135 **1.2.1. Homogeneous oxidation**

136 In addition to increasing the dissolution rate of iron, dissolved oxygen can be responsible for a change
137 in the corrosion mechanism: from dissolution to oxidation. Indeed, the formation of sodium chromite
138 (NaCrO₂) has been reported by several authors [27-29], particularly for oxygen concentrations higher
139 than ~15 µg g⁻¹ [14,30,31]. Scanning electron microscope (SEM) observations of the oxidized surfaces
140 indicate the formation of tetragonal crystals [14,32,33]. NaCrO₂ was characterised by X-ray Diffraction
141 (XRD) on ferrous alloys [31] and austenitic steels [14,30,33]. In each observation, a preferential
142 crystallographic orientation is reported along the [0001] axis. The oxide growth kinetic was measured

143 at 600 and 675 °C using the [0003] XRD peak intensity [30]. The oxide growth kinetic appears as
144 parabolic with time (Eq. 1.4):

$$145 \quad I_{XRD} = \sqrt{k_p \cdot t} \quad \text{Eq. (1.4)}$$

146 where I_{XRD} is the [0003] XRD peak intensity (without unit), k_p is the parabolic constant of oxide growth
147 (in s^{-1}) and t is time (in s). The parabolic constant equals to 5.10^{-3} h^{-1} at 600 °C and $\sim 2.10^{-2} \text{ h}^{-1}$ at 675 °C
148 for $23 \mu\text{g g}^{-1}$ of dissolved oxygen. The activation energy can be deduced by assuming an Arrhenius law
149 of k_p as a function of temperature (Eq. 1.5).

$$150 \quad k_p = k_{p_0} \cdot \exp\left(-\frac{Q_{k_p}}{RT}\right) \quad \text{Eq. (1.5)}$$

151 where k_{p_0} is a pre-exponential coefficient, Q_{k_p} is the activation energy of the parabolic constant of oxide
152 growth (order of magnitude $150,000 \text{ J mol}^{-1}$ [30]), R is the gas constant ($R = 8.314 \text{ J mol}^{-1} \text{ K}^{-1}$) and T is
153 the temperature (in K).

154 **1.2.2. Local corrosion and oxidation**

155 The formation of the NaCrO_2 oxide surface layer is not uniform. Pits are observed on the surface of
156 ferritic-martensitic steels [34,35] and intergranular corrosion is reported for ferritic-martensitic steels
157 [27,34-36] and austenitic steels at 650 °C [33] and 700 °C [37]. After 3100 h in flowing sodium at 710
158 °C containing $30 \mu\text{g g}^{-1}$ of oxygen and after 2500 h in flowing sodium at 300 °C containing $8,000 \mu\text{g g}^{-1}$
159 of oxygen, i.e in oxygen saturated sodium, intergranular corrosion was observed for 304L steel over
160 an extent of $40 \mu\text{m}$ [22]. Cavities are also observed on ferritic-martensitic steels [34-36] and austenitic
161 steels [33] immersed in liquid sodium containing oxygen at 650 °C. At 550 °C, local corrosion is not
162 observed for ferritic-martensitic steels immersed in liquid sodium containing $1 \mu\text{g g}^{-1}$ of oxygen [36].

163 **1.2.3. Chromium depletion**

164 Dissolved oxygen would also decrease the chromium composition of the steel surface layer [29,30,33-
165 36]. Our previous results [33] show that the oxidation of chromium into sodium chromite is the driving
166 force behind the diffusion of chromium to the steel surface. Cr depletion increases with time and
167 temperature. In the case of austenitic steels, Cavell and Nicholas noted that the values of the activation
168 energies of the parabolic constant of oxide growth and the diffusion of chromium in the grain boundaries
169 are close [30]. Consequently, they concluded that the chromium diffusion in the grain boundaries could

170 control the corrosion kinetics in sodium containing oxygen and then be the rate limiting step [30]. This
171 hypothesis would be consistent with our team's previous observations on local chromium depletion
172 around grain boundaries for the same grade of steel exposed under the same conditions except for the
173 higher temperature (650 °C) in liquid sodium containing about 200 $\mu\text{g g}^{-1}$ of dissolved oxygen [33].

174 **1.3. Summary and description of our experiments**

175 To conclude this short review, stainless steels and ferritic-martensitic steels are dissolved in liquid
176 sodium containing little oxygen. As oxygen concentration increases, the dissolution of iron and
177 chromium is enhanced by the formation of Na-Fe-O and Na-Cr-O complexes. These complexes increase
178 the corresponding solubility in liquid sodium. The formation of a soluble Na-Cr-O compound is a
179 hypothesis first proposed by Kolster and Bos [25]. For a slightly higher oxygen content, oxidation of
180 chromium into stable sodium chromite becomes possible. Previous literature has presented sometimes
181 contradictory observations on the actual formation of sodium chromite. The differences could be due to
182 competition from different mechanisms involved in such a system, or because of the somewhat different
183 operating conditions under which the tests were performed, or even the method applied to the storage
184 of specimens after the sodium tests. To our knowledge, there is no literature evidence of an observation
185 of NaCrO₂ oxide at the smallest scale currently available, nor of the observation of the dissolved Na-Cr-
186 O complex, nor of any relation between the Na-Cr-O complex and the NaCrO₂ oxide potentially
187 dissolved in the liquid sodium. The equilibrium concentration of Cr into sodium with steels is of the
188 highest importance on the Cr dissolution kinetics because small variations in equilibrium concentration
189 greatly change the modelled kinetics [38].

190 One of the conclusions of this review is that the role of chromium in the corrosion of austenitic steels
191 and its solubility in liquid sodium are not yet well understood. Our main objective is to study the
192 formation of sodium chromite on austenitic steels and its dissolution in liquid sodium.

193 In particular, the role of Na-Cr-O complex will be evaluated.

194 To this end, corrosion tests in liquid sodium were carried out under conditions that promote the
195 formation of sodium chromite and its dissolution. The ratio between the surface area of the specimens
196 and the sodium volume is low, which avoids saturating the liquid metal with Cr too quickly. In addition,
197 the test temperature was chosen at 550 °C to limit the iron dissolution, which would otherwise be too

198 severe to focus solely on the Cr oxidation [33]. The corrosion of 316L(N) austenitic steel was then
199 investigated at 550 °C in liquid sodium containing 200 $\mu\text{g g}^{-1}$ of dissolved oxygen for duration ranging
200 from 242 h to 7704 h.
201

202 **2. Materials, device, conditions and characterisation methods**

203 **2.1. Materials**

204 In the study presented here, the corrosion tests were performed on 316L(N) stainless steel provided by
205 Industeel France. Table 1 gives its composition, measured by glow discharge optical emission
206 spectroscopy (GDOES) for carbon and inductively coupled plasma atomic emission spectroscopy (ICP-
207 AES) for the other elements. The sample size was $30 \times 20 \times 1.5 \text{ mm}^3$ and the grain size was $41 \pm 2 \text{ }\mu\text{m}$
208 [33]. Before immersion in liquid sodium, all specimens were mechanically polished, the last step using
209 a $1 \text{ }\mu\text{m}$ diamond suspension (average roughness obtained $Ra < 0.1 \text{ }\mu\text{m}$, Bruker Contour GT
210 interferometer). The influence of surface roughness was not studied because a previous study showed
211 that it had no effect on oxidation results [33].

212 The sodium used for the corrosion tests was supplied by Métaux spéciaux S.A. Sodium is 99.95 wt.%
213 pure, containing $[\text{Ca}] < 2 \text{ }\mu\text{g g}^{-1}$, $[\text{Cl}] = 4 \text{ }\mu\text{g g}^{-1}$, $[\text{Fe}] = 1 \text{ }\mu\text{g g}^{-1}$, $[\text{K}] = 4 \text{ }\mu\text{g g}^{-1}$. It also contains C [33]
214 and is initially covered with a thick sodium oxide layer. This layer is manually removed inside a
215 glovebox filled with argon before the first melt.

216 **2.2. Corrosion test device**

217 The corrosion tests were performed in a static sodium device [33,39-41]. The stainless steel samples are
218 immersed in sodium (approximately 2.3 kg), contained in a molybdenum crucible. This crucible is
219 placed in a heat sink, the upper part of which opens inside a glovebox filled with purified argon. Sodium
220 is purified from its dissolved oxygen, first by removal of the floating oxides and then by hot trapping
221 [33]. Hot trapping consists of immersing a zirconium foil ($200 \times 300 \times 0.1 \text{ mm}$) at $650 \text{ }^\circ\text{C}$ for 3 days.
222 The oxygen concentration is then estimated to be less than $1 \text{ }\mu\text{g g}^{-1}$ [33]. Although this last purification
223 step is known to remove dissolved carbon from sodium, previous tests have indicated that the dissolved
224 carbon concentration remains high enough to cause the steel samples to carburize [33,39].

225 After purification, a precise amount of oxygen is added inside the liquid sodium by two methods. Either
226 sodium oxide powder ($\text{Na}_2\text{O} + 14.1 \text{ wt.}\% \text{ Na}_2\text{O}_2$, provided by Alfa Aesar) is dissolved in molten sodium
227 and the oxygen concentration is estimated assuming that the initial oxygen concentration in the liquid
228 sodium is equal to zero and that Na_2O and Na_2O_2 are completely dissolved in liquid Na. Or an argon-
229 oxygen gas mixture is added by bubbling. For this second method, the volume of oxygen gas added is

230 estimated from the measurement of the pressure variation in the Ar-O₂ bottle and the oxygen
231 concentration in liquid sodium is estimated assuming total oxygen absorption (this is confirmed by
232 measuring the partial oxygen pressure at the gas outlet). Uncertainties in the final oxygen concentration
233 in sodium is related either to the uncertainty of the sodium oxide weight or to the measurement of the
234 pressure variation of the bottle used for bubbling. Further details on the experimental setup are described
235 elsewhere [33]. Oxygen concentrations were measured by using the hot trap purification method, by
236 using the weight increase of the Zr foil that confirm the oxygen assessment within 20 %.

237 **2.3. Operating conditions**

238 The corrosion tests were performed at 550 °C with three different liquid sodium melts containing
239 approximately 200 µg g⁻¹ of oxygen. The objectives of the study were to investigate the influence of
240 immersion time (section 2.3.1) and to identify the reaction interfaces (section 2.3.2).

241 **2.3.1. Influence of immersion time**

242 The oxygen content of the first liquid sodium bath was set at $198 \pm 8 \mu\text{g g}^{-1}$ by dissolving the correct
243 amount of sodium oxide powder. Nine immersion times were chosen, namely 242, 584, 1276, 1924,
244 2395, 2830, 3842, 5304 and 7704 h, corresponding to nine samples. First, all nine samples were
245 immersed simultaneously in liquid sodium at 120 °C. Then, the sodium was heated to 550 °C at about
246 10 °C min⁻¹. After 242 h, the furnace was switched off, resulting in a temperature drop of 0.7 °C min⁻¹.
247 When the temperature reached 120°C, the first sample was taken out of liquid sodium. The exposure
248 time, 242 h for the first sample, is estimated from the moment when the temperature exceeds 97% of
249 the set temperature (i.e., 533 °C for a set temperature of 550°C). The furnace temperature is then raised
250 to 550°C to continue sodium corrosion of the remaining eight samples. To facilitate sample handling,
251 all samples are removed one after the other from the liquid sodium at 120 °C. This means that the n^{th}
252 sample ($1 < n < 9$) undergoes n temperature increases from 120°C to 550°C and n temperature decreases
253 from 550°C to 120°C. The exposure time is the cumulative time spent by the sample at temperatures
254 above 533°C.

255 In short, the samples undergo several cycles of temperature rise and fall. To validate this approach, the
256 corrosion mechanisms obtained were compared to the mechanisms obtained for samples immersed in
257 and removed from the bath at 550°C. For this, a second liquid sodium bath with an oxygen content of

258 $200 \pm 8 \mu\text{g g}^{-1}$ obtained by dissolving sodium oxide powder was used. Two samples were immersed for
259 242 and 584 h (in two periods of 242 and 342 h) with the same experimental protocol as previously
260 explained (including temperature rise and fall cycles). Two other samples were immersed in liquid
261 sodium at 550 °C. Both of them were removed from liquid sodium at 550°C as well, the first after 239
262 h and the second after 239 and 339 h, for a total immersion time of 578 h. The second sample was
263 immersed twice because the two samples were held onto the same Mo bar, allowing samples to be
264 immersed and removed at 550 °C.

265 **2.3.2. Reaction interfaces**

266 The third test is intended to further investigate the reaction mechanisms using oxygen isotopes ^{16}O and
267 ^{18}O to locate the reaction interfaces. We have implemented the so-called double oxidation technique,
268 often used to study the growth of oxide films at high temperature. The principle is to oxidize the metallic
269 substrate first under $^{16}\text{O}_2$ atmosphere then under an enriched atmosphere in ^{18}O [42-44]. To our
270 knowledge, this is the first time this technique has been used in the field of liquid sodium corrosion.

271 The experimental protocol is divided into four steps:

272 • In the first step, four samples were immersed at 120 °C in oxygen-free liquid sodium after purification
273 by zirconium hot trapping. The sodium was heated to 400 °C. Then, a gas mixture of argon and natural
274 oxygen (*Eurisotop*, 99.757 vol.% isotope of ^{16}O and 0.205 vol.% of ^{18}O , this ratio corresponds to the
275 natural abundance of each isotope) was bubbled for one hour to obtain an oxygen concentration of 200
276 $\pm 20 \mu\text{g g}^{-1}$. After bubbling, the ^{16}O -containing sodium was heated to 550 °C in 3 hours. The four samples
277 were maintained at temperatures greater than 533°C for 500 h. Then, the sodium was cooled to 120 °C
278 to remove the four samples from liquid Na. In short, these first four samples were corroded in ^{16}O -
279 containing sodium for 500 h.

280 • The sodium was again purified to an oxygen concentration of less than $1 \mu\text{g g}^{-1}$ by Zr hot trapping. A
281 gas mixture of argon and oxygen tracer (95 vol.% of isotope ^{18}O) was bubbled for one hour. The oxygen
282 concentration obtained was approximately $250 \mu\text{g g}^{-1} \text{ }^{18}\text{O}$, which corresponds to an equivalent ^{16}O
283 concentration of $280 \pm 20 \mu\text{g g}^{-1}$. The difference with the oxygen concentration in the other two sodium
284 baths is due to the difficulty of controlling the introduction of a precise amount of oxygen from the gas
285 bubbling.

286 • Three of the first four samples were re-immersed in this molten Na bath. The sodium was heated to
287 550 °C and the samples were removed one by one after 100, 500 and 960 h total immersion time with
288 the same experimental protocol as previously explained (including cycles of temperature rise to 550°C
289 and fall down to 120°C). These three samples were then immersed for 500 h in ¹⁶O -containing sodium
290 and then for 100, 500 and 960 h in ¹⁸O -containing sodium.

291 **2.4. Characterisation techniques**

292 After corrosion in liquid sodium, all samples were immersed in 99.9 wt.% pure ethanol (provided by
293 Carlo Erba) at room temperature for one hour. Interaction with ethanol removes sodium residues from
294 samples surface. The samples are then characterized by complementary techniques.

295 Specimens were weighed before and after the corrosion test (AT20 precision balance, Mettler Toledo).

296 The phases formed during corrosion on the surface of the samples were characterised by X-Ray
297 Diffraction (XRD, Bruker D8 discover) in the θ -2 θ configuration with a copper cathode emitting X-rays
298 of wavelength $\lambda = 1.5406 \text{ \AA}$. Scanning Electron Microscopy (SEM, Zeiss LEO 1460VP) combined with
299 Energy Dispersive X-ray spectroscopy (EDX, SAMX DXP-X10P) was used to observe and analyse the
300 surfaces and polished cross-sections of the specimens. All samples were weighed and observed by SEM
301 and most samples were characterised by XRD.

302 For experiments using oxygen isotopes, mean elementary depth profiles were obtained on a 4 mm
303 diameter disk from the sample surface using Glow Discharge Optical Emission Spectroscopy (GDOES,
304 GD-Profilier 2, Horiba Scientific) under the same conditions as those presented before [33]. Each
305 analysis with GDOES was repeated at least twice. A precise calibration procedure with a set of standards
306 makes it possible to convert the element intensities into compositions with a fairly high confidence for
307 most elements, with the exception of oxygen and sodium whose variations are only qualitative.
308 Elementary depth profiles were also obtained by Secondary Ion Mass Spectrometry (SIMS, IMS7f,
309 Cameca). The incident beam ions used were Cs⁺ for oxygen isotope and O₂⁺ for metallic elements. The
310 incident beam energy was 15 keV and the secondary ion beam energy 5 keV. Only negative ions were
311 analysed. The analysis were performed on a 150 μm square divided in 128 x 128 pixels. The depth of
312 the craters at the end of the GDOES and SIMS analysis was obtained using an optical interferometer
313 (Contour GT, Bruker). Only the samples obtained during the corrosion test using the oxygen isotopes

314 were characterised by SIMS and GDOES. Only one of these samples (1460 h of cumulated immersion
315 time) was also characterized by Transmission Electron Microscopy (TEM) in scanning mode. The
316 instrument (Tecnai Osiris TEM, FEI) is coupled with an EDX detector (ChemSTEM EDX, FEI). The
317 sample was prepared by Focused Ion Beam (FIB, Strata 400S FIB, FEI).

318

319 **3. Corrosion test results**

320 The mass gain of samples immersed in liquid sodium containing $200 \mu\text{g g}^{-1}$ of oxygen at 550°C is given
321 as a function of immersion time in Figure 1. All samples show a mass gain. Up to 3842 h of immersion,
322 the mass gain appears almost negligible, although positive, and limited to about $0.5 \cdot 10^{-3} \text{ kg m}^{-2}$ (the mass
323 gain measured for a sample is divided by its total surface area including the 2 faces and 4 edges). This
324 result is remarkably reproducible for all three tests up to 1460 h of immersion in liquid sodium. After a
325 transition between 3842 h and 5304 h, the mass gain increased significantly to $2.2 \cdot 10^{-3}$ and $2.5 \cdot 10^{-3} \text{ kg}$
326 m^{-2} for 5304 h and 7704 h of immersion respectively.

327 As explained in the experimental protocol (Section 2.3), most samples underwent several cycles of
328 temperature rise and decrease to facilitate sample handling. The mass gain of two samples immersed in
329 and removed from the bath at 550°C was measured (\otimes in Fig. 1). The results obtained are in very good
330 agreement with the other samples, thus validating our protocol and excluding significant precipitation
331 on the specimen during the cooling stage.

332 The expected corrosion mechanisms for stainless steel in liquid sodium are (1) dissolution which would
333 result in mass loss and (2) penetration of the liquid metal into the micro-porosities, diffusion of oxygen
334 and carbon to their solubility limits in the matrix and then nucleation and growth of oxides and carbides
335 on the steel surface and subsurface, which result in mass increase. The large increase in mass gain after
336 several thousand hours should be the result of a change in corrosion mechanisms. This is why we will
337 focus first on the characterization of samples immersed during 242 h to 3842 h (Section 3.1) and then
338 on samples immersed during 5304 and 7704 h (Section 3.2).

339 **3.1. Immersion time less than 4000 h**

340 For the samples immersed in liquid sodium containing $200 \mu\text{g g}^{-1}$ of oxygen at 550°C for less than 4000
341 h, the mass gain is positive and low (Fig. 1). In most of the examples selected here, the results will be
342 presented for the sample immersed for 1460 h in the third liquid sodium bath (section 2.3). The results
343 for this immersion time are representative of all immersion times less than or equal to 3842 h.

344 **3.1.1. Phases characterisation**

345 The phases detected on austenitic steel in liquid sodium containing $200 \mu\text{g g}^{-1}$ of oxygen at 550°C are
346 identified by XRD. The diffraction pattern obtained for a 1460 h immersion time is plotted as the dark

347 line at the bottom of Fig. 2 and superimposed with the diffraction patterns of NaCrO₂ (PDF file # 00-
348 025-0819), austenite (PDF file # 031-0619) and Fe₃Mo₃C (PDF file # 00-047-1191).

349 The initial material corresponding to the austenite matrix is detected by the presence of the two most
350 intense peaks (43.772°, 50.987°). The less intense peaks expected for austenite do not appear (24.858°,
351 35.438°, 57.531°).

352 Molybdenum-iron carbide (Fe₃Mo₃C) is identified by the following group of peaks, 35.087°, 39.598°,
353 42.112° and 46.047°, the less intense peaks (32.121°, 49.016°, 54.595°, 59.176°) being lost in the
354 background noise. It should be noticed that all M₆C type carbides have about 3 Mo atoms and 3 M atoms
355 which can be Cr, Mn, Fe and Ni in variable proportions. The best fit was found for Mo₃Fe₃C.

356 The theoretical peaks of NaCrO₂ are also plotted on the diffractogram, as they can correspond to the
357 broadened peaks observed at 16.7° and 21.3°. The [0003] plane of NaCrO₂ should present a diffraction
358 peak at 16.651°. However, the parallel crystallographic plane [0006] expected at 33.64° is not present,
359 nor are the other crystallographic planes (35.279°, 36.635°, 41.705°, 45.187°, 53.649°, 58.438°).

360 Crystallized NaCrO₂ is therefore not clearly characterised even if small amounts of an amorphous phase
361 (large peaks between 15 and 25°) could correspond to sodium chromite.

362 **3.1.2. External oxidation and carburization**

363 After corrosion in liquid sodium containing 200 µg g⁻¹ of oxygen, the steel surfaces are characterised by
364 SEM. The backscattered electron images obtained at two different locations are shown in Fig. 3 for the
365 sample immersed for 1460 h. The contrast differences of these images give information about the
366 chemical composition of the phases (the brighter a zone appears, the higher its atomic number). The
367 steel surface is covered with dark grey particles about 200 nm in diameter. Their surface density varies
368 from place to place, possibly in relation to the orientation of the underlying austenite grains, forming
369 either discrete particles (Fig. 3a) or a continuous layer (Fig. 3b). The steel surface can be seen in light
370 grey between these dark grey particles (example of black arrow, Fig. 3a). White particles of about 1 µm
371 in diameter are also observed.

372 Chemical analysis were performed by EDS in the square area of Fig. 3b. Elementary maps of oxygen,
373 sodium, chromium, iron, nickel and molybdenum are given in Figs. 4a, b, c, d, e and f respectively.

374 Areas with a high concentration of the element appear in white. The layer of small particles 200 nm in

375 diameter contains O, Na and Cr (Figs. 4a, b and c). The white particles, shown in Fig. 3, are rich in
376 molybdenum (Fig. 4-f) and do not contained O, Na and Cr. Fe and Ni are detected almost everywhere
377 and correspond mainly to the steel matrix (Figs. 4d and e). The iron composition is higher in areas where
378 O, Na and Cr compositions are weak (top right for example), probably because the layer of corrosion
379 products is thinner.

380 Based on the results of these characterizations, the steel is coated with a thin, non-homogeneous
381 corrosion layer, resulting in the low measured mass gain (Fig. 1). This layer contains sodium chromite
382 in the form of dark grey particles 200 nm in diameter as can be deduced from their composition and
383 shape [14,33]. White particles 1 μm in diameter should correspond to M_6C carbide, characterised by
384 XRD, since they are rich in Mo and C cannot be detected by EDX in our conditions.

385 To complete the surface characterisations, various techniques were used to measure the chemical
386 evolution of the material under its surface: (1) mean composition as a function of the distance to the
387 surface by GDOES (sections 3.1.3 and 3.1.4), (2) fine characterization of the Cr content around a grain
388 boundary by TEM/EDX on a thin cross section extracted by FIB technique (3.1.4) and (3) position of
389 the reaction interface by SIMS based on the analysis of ^{18}O tracers (3.1.5).

390 **3.1.3. Internal oxidation and carburization**

391 Figure 5 shows the compositions of C, O, Na, Cr, Mn, Fe, Ni and Mo in log-scale as a function of
392 sputtered depth from the steel surface up to 5 μm depth, where the composition corresponds to the initial
393 steel composition. The example chosen corresponds to the sample immersed for 1460 h at 550 $^\circ\text{C}$ in
394 liquid sodium with an oxygen content of 200 $\mu\text{g g}^{-1}$.

395 At the steel surface, the average composition is enriched in O, Na and Cr in a 0.75 μm -thick layer. For
396 the first 0.4 μm , the sodium content exceeds 40 at.% while the oxygen content is steadily decreasing.
397 The chromium composition increases from the steel surface to 0.15 μm , decreases from 0.15 μm to 0.75
398 μm where it presents a local minimum. This surface layer rich in O, Na and Cr corresponds to the sodium
399 chromite zone. In this zone, the molybdenum content increases to a maximum located at a depth of 0.19
400 μm , while carbon presents a high content that decreases from the surface to 1 μm . At this depth, a change
401 in slope of the C concentration profile is noticed and the Mo content reaches its bulk content. This
402 surface layer, enriched with Mo and C, should correspond to the zone where M_6C carbides are formed.

403 Iron and nickel compositions are steadily increasing from the steel surface, probably due to the
404 inhomogeneity of the corrosion zone and the roughness of the interface. It should be noticed that
405 chromium depletion is greater and deeper than iron depletion and that iron depletion is greater than
406 nickel depletion (this is clearly highlighted with the Fe/Ni ratio, not shown here). One corrosion
407 mechanism proposed in the literature is the preferential dissolution of nickel [1,6,8]. This is probably
408 not the case under our corrosion conditions, since, if nickel were preferentially leached from austenite,
409 Ni depletion would have been higher than that of Fe. In addition, it can be noted that the depletion in Cr
410 composition from 1 to 2.5 μm from the steel surface corresponds to the second peak of the sodium
411 profile. This second sodium peak could correspond to internal oxides formed at the grain boundaries (as
412 was the case at 650 $^{\circ}\text{C}$ [33], which shows significant similarities in the element profiles measured).
413 Finally, the corrosion zone consists of two parts: a surface layer composed of sodium chromite and
414 carbides and a corrosion affected zone composed of austenite depleted in Cr. For this last reason, the
415 role of Cr was further investigated and the results are presented in Section 3.1.4.

416 **3.1.4. Role of Cr**

417 *In-depth characterization of the average Cr content of corroded steel*

418 In order to evaluate the influence of the immersion time on the Cr depletion, three Cr concentration
419 profiles are plotted in Fig. 6 for 500, 1000 and 1460 h of immersion time. For the sake of comparison,
420 the interface between the corrosion zone (sodium chromite) and the steel matrix is chosen to be the
421 origin of the x -axis and is assumed to be located at the minimum chromium composition (1000 or 1460
422 h) or at a slope change in the Cr profile (500 h). With this procedure, negative depths ($x < 0$) correspond
423 to the zone where NaCrO_2 is formed. The extent of this corrosion zone increases slightly with exposure
424 time: 0.35, 0.43 and 0.67 μm for respectively 500 h, 1000 h and 1460 h. At the same time, the extent of
425 the austenite zone depleted in Cr also increases. The low mass gain of the sample observed at the
426 beginning of the test corresponds to the formation of a thin layer of sodium chromite associated with the
427 chromium depletion zone.

428 *Chemical composition in Cr around a grain boundary*

429 A thin foil from a cross-section of the sample immersed for 1460 h at 550 $^{\circ}\text{C}$ in liquid sodium with 200
430 $\mu\text{g g}^{-1}$ of oxygen was obtained by FIB and observed by STEM in order to accurately characterise

431 chemical variations around the grain boundary. Fig. 7 gives a large field of view of the sample and the
432 inset image provides a larger magnification of the grain boundary emerging at the steel surface. Fig. 8
433 shows the elementary cartography of the enlarged zone for O, Na, Cr, Fe, Ni and Mo.

434 In order to protect the sample during the shaping of the thin foil, a layer of tungsten was deposited on
435 the surface exposed to sodium (at the top of the image, Fig. 7). Under the protective tungsten layer, a
436 thin layer of faceted particles (300 nm) is observed on the surface of the grains. Some of these particles
437 are darker than the alloy, others lighter. According to the elementary maps (Fig. 8), the dark particles
438 contain O, Na and Cr. The clear particles contain Fe and Mo. They correspond respectively to NaCrO_2
439 in the form of a thin and non-homogeneous layer on the surface of the sample and to M_6C particles
440 (since they may contain Fe [33]). It is also noted that above the particle of M_6C , enrichments in O, Na
441 and Fe are detected: no candidate other than the Na_4FeO_3 ternary oxide can be proposed, although it
442 should not be stable in the test conditions.

443 One of the M_6C particles is located at the top of the grain boundary on the sample surface. Along the
444 grain boundary and below the surface, we see a first phase rich in Mo and Fe and then a large phase rich
445 in O, Na and Cr (300 nm wide, 1 μm long), which corresponds to an internal NaCrO_2 oxide. The NaCrO_2
446 particle presents slip bands, cracks and cavities that were filled with sodium during immersion in liquid
447 sodium. Further below the enlarged area, a black area 0.5 μm long contains Si and O (indicated by an
448 EDS point analysis not shown here) that may correspond to silicon oxide (SiO_2), indicating that internal
449 oxidation may occur. This issue will not be discussed further. Further down the grain boundary, small
450 clear particles, corresponding to carbides, are observed, but their precise chemical characterizations has
451 not been possible. Finally, the grain boundary ends with a triple grain boundary at a depth of 16.3 μm .

452 It can be noted that these observations, although local, are consistent with the GDOES mean
453 measurement (Figs. 5 and 6) as well as with the SEM observations (Fig. 3). Indeed, the surface corrosion
454 layer containing chromite and carbides presents a thickness of 300 nm in accordance with the 200 nm
455 crystallites observed with SEM. The area affected by corrosion below the surface layer corresponds to
456 grain boundaries that contain carbides and oxides to a depth of about 2 μm . This depth is in fairly good
457 agreement with the GDOES mean measurement of 2.5 μm for the Cr depleted zone.

458 In order to accurately quantify the extent of chromium depletion along this specific grain boundary,
459 several chromium EDX profiles were measured at different locations shown by the arrows in Fig. 7.
460 Profiles 1, 2, 3 and 4 were measured in the direction perpendicular to the grain boundary, at an increasing
461 distance from the sample surface of 0.52, 4.26, 7.67 and 12.79 μm respectively. The chromium profiles
462 obtained, expressed in at.%, are plotted in Fig. 9. The origin of the abscissa corresponds to the grain
463 boundary position. Cr profiles close to the sample surface exhibit a higher chromium depletion
464 compared to profiles located at a greater distance. The chromium composition is always minimal at the
465 grain boundary. This minimum gradually increases from 2.7 at.% close to the sample surface to 7 at.%
466 and 10.5 at.% deeper. The Cr depletion in profile 1 appears to be asymmetric: it extends over 75 nm from
467 the left grain boundary while the depletion of the right grain extends up to 440 nm. These observations
468 are reproduced on profiles 2 and 3 with shorter depletion distances and higher minimum compositions.
469 On profile 4, the asymmetry is no longer visible. Depletion along the grain boundary and asymmetry
470 between the grains are typical of the consumption of an element diffusing to the interface. Diffusion in
471 grain boundaries is faster than volume diffusion, because the grain boundaries present a higher degree
472 of disorder [45]. Similarly, the asymmetry may be explained by the fact that the bulk diffusion
473 coefficient depends on grain orientation or other mechanisms such as grain-boundary migration.

474 **3.1.5. Interface reaction**

475 In order to study the oxidation mechanism, the oxygen tracer technique was used in the third test (section
476 2.3.2). For this test, oxygen was added to the liquid sodium by bubbling a gas either composed mainly
477 of ^{16}O (99.757 vol.%) and 0.205 vol.% of ^{18}O or composed of 95 vol.% of the stable isotope ^{18}O . Three
478 samples were successively immersed in liquid sodium containing $200 \mu\text{g g}^{-1} \text{ }^{16}\text{O}$ for 500 h, then in liquid
479 sodium containing $250 \mu\text{g.g}^{-1} \text{ }^{18}\text{O}$ (corresponding to $280 \mu\text{g g}^{-1} \text{ }^{16}\text{O}$) for 100, 500 and 960 h. A fourth
480 sample that has only been immersed for 500 hours in liquid sodium containing $200 \mu\text{g g}^{-1} \text{ }^{16}\text{O}$ is used as
481 a reference. The SIMS technique using mass spectroscopy makes it possible to differentiate the ^{16}O and
482 ^{18}O signals. In addition, it provides the intensities of the detected elements in all three directions of
483 space, allowing isotope mapping as a function of sputtered depths.

484 Fig. 10 provides cartographies of the relative intensities of ^{18}O (Fig. 10, top) and ^{16}O (Fig. 10, bottom)
485 at several depths from the sample surface. The chosen example was obtained for an immersion time of

486 1460 h (the same results were obtained for the lower immersion times studied). The cartographies are
487 squares 150 μm wide, composed of 128 pixels in each direction. In Fig. 10, at 0.02 μm depth, near the
488 surface, the ^{18}O signal is high, implying that the surface is covered with oxide, some areas had a weak
489 ^{18}O signal, such as the upper left corner which appears free of oxide. At 0.6 μm below the surface,
490 heterogeneities of oxide thickness appear: some areas are covered with oxide while others are not. At
491 depth, the free oxide zones extend and delimit the alloy grain boundaries (1.4 μm deep). The evolution
492 of the ^{16}O concentration as a function of depth is identical. It seems that the concentration of ^{18}O is
493 higher than that of ^{16}O at a depth of 1.4 μm .

494 In Fig. 10, two square areas (20 μm x 20 μm) are visible, one above one grain and the other including a
495 grain boundary. For each of these square areas, the ^{16}O and ^{18}O concentration profiles were measured as
496 a function of corrosion time. Fig. 11 presents the results obtained in the grains (left column, Fig. 11a,
497 11c and 11e) and at the grain boundaries (right column, Fig. 11b, 11d and 11f) for 600 h (Fig. 11a and
498 11b), 1000 h (Fig. 11c and 11d) and 1460 h (Fig. 11e and 11f). The oxygen profiles are compared with
499 the ^{16}O profile obtained in the first corrosion step (500 h in ^{16}O containing liquid sodium, black dotted
500 line). For each corrosion time, the oxygen (^{16}O and ^{18}O) concentration and oxidation depth are higher in
501 the grain boundaries than in the grains. The ^{18}O concentration increases with corrosion time both in the
502 grains and at the grain boundaries. The ^{16}O concentration is of the same order of magnitude as that
503 obtained for the reference case but it seems to increase slightly with corrosion time. As the second
504 corrosion step involves only ^{18}O , this increase is probably due to a slight progressive pollution of liquid
505 Na in ^{16}O .

506 From the measurements of ^{16}O and ^{18}O , the relative abundance of ^{18}O can be calculated as a function of
507 depth from the surface (Fig. 12). The relative abundance of ^{18}O is calculated as the ratio of the intensity
508 of ^{18}O signal $I(^{18}\text{O})$ to the sum of the intensities of the ^{16}O and ^{18}O signals $I(^{18}\text{O}) + I(^{16}\text{O})$. The same
509 measurements were performed at the different immersion times (600, 1000 and 1460 h). Fig. 12 shows
510 the relative abundance profile of ^{18}O from the surface to 2.5 μm deep in a grain (Fig. 12a) and on a grain
511 boundary (Fig. 12b). As the intensities of the measured signals decrease with depth, the ends of the
512 relative abundance profiles are noisy. In the grain (Fig. 12a), depths between 0 and 0.1 μm are enriched
513 in ^{18}O . This peak in ^{18}O abundance increases and widens with immersion time. Between 0.1 and 0.3 μm

514 deep, the ^{18}O abundance also increases with immersion time. For depths greater than $0.3\ \mu\text{m}$, the
515 intensity of the oxygen signals is too low, resulting in a noisy relative abundance profile. At the grain
516 boundary (Fig. 12b), the ^{18}O abundance profiles show a peak that extends to $0.3\ \mu\text{m}$ and increases in
517 height with immersion time (as in the grain, Fig. 12a). From a depth of $0.5\ \mu\text{m}$, ^{18}O becomes more and
518 more abundant over time to a depth of $1.7\ \mu\text{m}$. As reminded above, the volume fraction of ^{18}O compared
519 to ^{16}O in the gas mixture was low (0.205 vol.%) during the first 500 h and then higher (100 vol.%). This
520 means that if the relative abundance of ^{18}O is greater than 0.00205, the diffusion of ^{18}O into the steel
521 occurred after the first 500 h of immersion in sodium. As shown in Fig. 12, the relative abundance of
522 ^{18}O is greater than 0.00205 in both the grain and the grain boundary.

523 Most of the time, the double-oxidation technique is used to study the transport mechanism during the
524 oxide scale growth at high temperature [42-44]. In our case, the oxide scale remained very thin for
525 immersion times of less than 4000 h and the oxide was mainly located at the grain boundaries. This case
526 is much less documented in the literature [46]. Two mechanisms determine the oxygen isotope
527 distribution in the material, namely diffusion transport and oxygen isotope substitution in already formed
528 oxide particles.

529 Fast oxygen diffusion along the austenite grain boundaries is clearly visible throughout the immersion
530 period (Fig. 12b). Much of ^{18}O passes through the region of the ^{16}O -oxides previously formed along the
531 grain boundaries that serve as fast oxygen transport channels through the internal precipitate zone,
532 resulting in an increased amount of ^{18}O -oxides near the oxidation front. This behavior has also been
533 observed in the case of selective oxidation of model ternary iron-based alloys containing Mn and Al, Cr
534 or Si at 700°C for 60 min in Ar / H_2 / H_2O gas mixture [46].

535 At the sample surface, a peak of ^{18}O relative abundance can be observed. This could be explained by
536 two mechanisms. For the first mechanism, when diffusing into the materials, ^{18}O comes into contact
537 with ^{16}O -containing oxides. This could cause a tracer exchange and near the sample surface, the
538 exchange time is longer, leading to a ^{18}O maximum concentration. The ^{16}O isotope would then be pushed
539 further inside the steel giving the shape of the ^{16}O profile measured after 1000 h of corrosion time (Figs.
540 11c to 11f). This interpretation should be taken with caution due to the slight ^{16}O pollution mentioned

541 above. The second mechanism involves the formation of a new oxide scale due to Cr diffusion to the
542 steel surface.

543 **3.2. Immersion time more than 5000 h**

544 The mass of samples immersed for 5304 and 7704 h increased 5 times more than that of samples
545 immersed for a shorter period of time (Fig. 1). The sharp increase in mass gain after several thousand
546 hours is the result of a change in corrosion mechanisms.

547 First, the XRD phase characterisation of the 5304 h immersed sample (blue line in Fig. 2) shows the
548 formation of M_6C as for shorter immersion times. In addition, $NaCrO_2$ diffraction peaks are also present
549 at angles $2\theta = 16.651^\circ, 33.64^\circ, 35.279^\circ, 36.635^\circ, 41.705^\circ, 53.649^\circ$ and 58.438° . Two other peaks are
550 observed at $2\theta = 12.49$ and 22.68° , which could not be explained. This characterisation proves the
551 formation of crystallized $NaCrO_2$ after 5304 h of immersion in liquid sodium.

552 This is confirmed by the characterization of cross-section samples. For example, the cross-section of a
553 sample immersed for 7704 h in liquid sodium containing $200 \mu g g^{-1}$ of oxygen at $550^\circ C$ is given in Fig.
554 13. It shows the secondary electron image of the cross-section and the elementary EDX mapping of O,
555 Na, Cr, Fe and Mo. At the top of Fig. 13a, the mounting resin appears in black, at the bottom stainless
556 steel appears in grey. At the interface, a dark grey phase and a light grey phase are visible. These two
557 phases extend to a depth of $4 \mu m$. According to the EDX analysis, the dark grey phase is $NaCrO_2$ and
558 the lighter phase is M_6C containing Mo and Fe. Compared to the results obtained after 1460 h of
559 immersion (Fig. 7), the corrosion products are thicker and continuous at longer immersion times: the
560 surface is covered by $NaCrO_2$ and M_6C .

561

562 **4. Discussion on corrosion mechanisms in liquid sodium**

563 **4.1. Formation of sodium chromite**

564 Two oxidation behaviours were observed with mass gain measurements (Fig. 1).

565 For short immersion times (less than 4000 h), a small mass increase is measured. SEM and TEM
566 analyses show the formation of NaCrO₂ (Figs. 3, 4, 7 and 8): in this condition, NaCrO₂ is formed below
567 the surface at the grain boundaries and a very thin and discontinuous layer probably forms on the steel
568 surface. X-ray diffraction does not detect it, probably because of the small amount formed (Fig. 2).

569 For longer immersion times (more than 4000 h), a larger mass increase is measured and NaCrO₂ is
570 detected by all characterisation methods.

571 Two hypotheses can be formulated and tested: NaCrO₂ is formed for all immersion times but, for the
572 short immersion times, it dissolves as it is formed.

573 **4.1.1. Consistency of the NaCrO₂ formation hypothesis**

574 *Thermodynamic stability under the selected experimental conditions*

575 Thermodynamic calculations of oxide stability in the same system as used here can be found in ref. [33]
576 (Ellingham diagram, Fig. 10 [33]). In particular, for the same austenitic steel, i. e. the same Cr activity,
577 it can be seen that NaCrO₂ is stable at a temperature above 350°C if the composition of the liquid sodium
578 in dissolved oxygen is of the order of 200 µg g⁻¹ (precisely 189 µg g⁻¹ in the publication). These
579 thermodynamic data therefore predict that NaCrO₂ can be formed on the austenitic steel considered here
580 in liquid sodium containing 200 µg g⁻¹ of oxygen at 550°C.

581 *Consistency with experimental results obtained at short immersion time*

582 For an immersion time of 3842 h or less, SEM observations show that NaCrO₂ forms a discontinuous
583 layer of 200 nm large crystals (Fig. 3). For these immersion times, the mass gain of the samples varies
584 little and is equal to $\Delta m_s = (2.0 \pm 0.3) 10^{-4} \text{ kg m}^{-2}$. Assuming that the mass variation of the samples is
585 due only to the formation of NaCrO₂, the thickness of a continuous oxide layer corresponding to this
586 mass gain can be calculated using Eq. 4.1.

$$587 \quad e_{\text{NaCr}_2} = \frac{1}{\rho_{\text{NaCrO}_2}} \Delta m_s \quad \text{Eq. (4.1)}$$

588 where ρ_{NaCrO_2} is the sodium chromite density ($\rho_{NaCrO_2} = 4,360 \text{ kg m}^{-3}$ [33]). A thickness of $e_{NaCrO_2} =$
589 $46 \pm 7 \text{ nm}$ is obtained. This calculation overestimates the continuous oxide layer thickness equivalent to
590 the mass gain of the samples, since it does not take into account the M_6C formation which also
591 contributes to the mass gain. In conclusion, the size of the crystals (200 nm) combined with their
592 dispersion is consistent with the order of magnitude of the equivalent thickness of the oxide found.

593 **4.1.2. Consistency of the $NaCrO_2$ dissolution hypothesis**

594 As shown in Figs. 5 and 6, the austenitic steel is depleted in chromium below its surface: the surface
595 oxide corresponds to the chromium peak associated with the high Na and O composition. As the distance
596 to the surface increases, the Cr composition decreases until a minimum concentration, corresponding to
597 the depletion zone, is reached and then increases to the bulk composition measured at 17 at.%.
598 Consequently, the Cr concentration profiles obtained are compatible with Cr selective oxidation, i.e. the
599 diffusion of Cr to the steel surface and its oxidation into $NaCrO_2$.

600 Using the shape of the concentration profiles obtained by GDOES and assuming that there is no receding
601 of the interface, we can estimate the amount of Cr that has left the austenitic steel in this process. The
602 measurements give the chromium composition in mole fraction (x_{Cr}) as a function of depth (z) from 0
603 (corresponding to the minimum Cr concentration) to ∞ (corresponding to the initial composition x_{Cr}^0)
604 (Fig. 6). The total amount of Cr consumed in steel per unit area (mol m^{-2}), $\frac{\Delta n_{Cr}}{S}$, can be calculated by

605 Eq. 4.2:

$$606 \quad \frac{\Delta n_{Cr}}{S} = \int_0^{\infty} (x_{Cr}^0 - x_{Cr}(z)) \frac{\rho(z)}{M(z)} dz \quad \text{Eq. (4.2)}$$

607 where $\rho(z)$ is the density of the material at depth z and is given by GDOES, $M(z)$ is the molar weight
608 at depth z , such that $M(z) = \sum_i x_i(z) M_i$, where $x_i(z)$ is the mole fraction of element i at depth z and
609 M_i is the molar mass of element i . In practice, $\rho(z)$ and $M(z)$ are almost constant and equal to $\rho(z) =$
610 $(7.5 \pm 0.2) 10^3 \text{ kg m}^{-3}$ and $M(z) = (54 \pm 2) 10^{-3} \text{ kg mol}^{-1}$.

611 This amount of released Cr corresponds to an equivalent thickness of oxide that can be formed, given
612 by Eq. 4.3. It should be noted that, due to the increase in Cr depletion (Fig. 6), the thickness of the oxide
613 formed is expected to increase over time, which is contradicted by short-term mass gain measurements.

614
$$e_{NaCrO_2} = \frac{\Delta n_{Cr} M_{NaCrO_2}}{S \rho_{NaCrO_2}} \quad \text{Eq.(4.3)}$$

615 where $M_{NaCrO_2} = 107 \cdot 10^{-3} \text{ kg mol}^{-1}$ is the molar weight of $NaCrO_2$.

616 The $NaCrO_2$ thickness calculated with Eq. 4.3, i.e. assuming that the Cr released from the steel is
 617 completely oxidized into a compact $NaCrO_2$ layer, is between at least 138 nm for 242 h of immersion
 618 in liquid sodium and 670 nm for 3842 h. The equivalent oxide thickness obtained by mass gain is $46 \pm$
 619 7 nm at most (section 4.1.1). Since the oxide thickness possibly formed by the Cr released from the steel
 620 is greater than the measured oxide thickness, it can be concluded that only part of the chromium from
 621 the steel reacted on the surface to form sodium chromite and that the remaining part of Cr was released
 622 into the liquid sodium. As the Cr solubility in liquid sodium is far too low to justify any selective
 623 leaching, it must be concluded that the Cr was released into the liquid sodium under a specific but
 624 unidentified chemical compound.

625 **4.1.3. Proposed reaction mechanisms**

626 As explained above, the shape of the Cr composition profiles confirms the transport of chromium from
 627 the steel bulk to its interface with liquid sodium (Fig. 6). In addition, the shape of Cr depletion around
 628 grain boundaries (Fig. 9) is typical of the diffusion of type B regime according to Harrison's
 629 classification [47], which implies that grains and grain boundaries participate in the diffusion
 630 mechanisms [48-52]. This type B diffusion regime explains the presence of thicker oxide within the
 631 grain boundaries than at the grain surface. This chromium which diffuses towards the surface of the steel
 632 can form $NaCrO_2$ or dissolve in liquid sodium (section 4.1.2).

633 The formation of $NaCrO_2$ crystals may result (i) from heterogeneous precipitation of dissolved Cr or
 634 compounds containing Cr in liquid sodium or (ii) from selective oxidation of Cr diffusing from the steel
 635 bulk to the steel/oxide interface.

636 In the first case, the driving force for heterogeneous precipitation is the chemical supersaturation of
 637 liquid sodium into Cr or compounds containing Cr. Under our conditions, supersaturation can only be
 638 achieved during the cooling phase (from 550 °C to ambient temperature), which implies that $NaCrO_2$
 639 formation would only occur during cooling. If this were the case, the samples that undergo this cooling
 640 phase would present a larger mass gain than a sample taken from liquid sodium at 550 °C without such

641 a decrease in temperature in liquid sodium. Experiments show that the mass gain for samples taken
642 directly from liquid sodium at 550 °C (⊗ in Fig. 1) is close to that of samples subjected to temperature
643 transients (● in Fig. 1). It therefore appears that mass gain is not affected by temperature transients and
644 that NaCrO₂ formation does not result from heterogeneous precipitation of Cr or a compound containing
645 Cr, from liquid Na.

646 Consequently, NaCrO₂ formation results from the reaction of sodium and oxygen dissolved in Na with
647 chromium in steel. This mechanism is confirmed by the location of the oxidation reaction, in particular
648 in the steel grain boundaries, determined by the double oxidation technique with oxygen isotopes (Figs.
649 11 and 12, section 3.1.5). This is also supported by the constant Cr composition observed at the
650 NaCrO₂/steel interface (x_{Cr}^i) independently of immersion time with $x_{Cr}^i = 9.6 \pm 0.5$ at.% (Fig. 6). This
651 composition should coincide with the Cr composition in equilibrium with NaCrO₂ if the GDOES
652 technique allowed a local value to be measured rather than the mean value over a large surface area [33].
653 The Cr composition gradient measured in steel (Fig. 6) is representative of a positive diffusion flux of
654 Cr to the surface. Therefore, the oxide thickness was expected to increase over time. However, the mass
655 of oxide formed is almost constant during the first 3842 hours. This can be explained by the dissolution
656 of NaCrO₂ simultaneously with its formation or the dissolution of Cr in liquid sodium. This NaCrO₂
657 dissolution was demonstrated by the difference in the amount of Cr released by the steel and the Cr
658 contained in oxide (section 4.1.2).

659 So far, only Cr oxidation and depletion have been taken into account for the mass balances. In the next
660 section, the dissolution of the alloying elements in Na will be evaluated.

661 **4.2. Mass balance considering dissolution, oxidation and Cr depletion in steel**

662 **4.2.1. Driving force for dissolution**

663 According to previous studies [7-14], dissolution is recognised as the main corrosion phenomenon of
664 austenitic steel in flowing liquid sodium. The driving force of dissolution is the difference between the
665 concentration of the element in liquid Na and its solubility. The solubility of an element in liquid sodium
666 is defined as the highest concentration of that element in dissolved form. The known solubilities are
667 those of pure elements, such as C [1], O [53], Cr [54], Mn [55], Fe [56], Ni [57], Mo [1]. In the case of

668 Cr, solubility ($w_{Cr,ppm}^{Na,sat}$, in $\mu\text{g g}^{-1}$) is given for temperatures (T in $^{\circ}\text{C}$) between 683 and 980 $^{\circ}\text{C}$ by [54]:

669 $\log w_{Cr,ppm}^{Na,sat} = 9.35 - \frac{9010}{T+273.15}$. By assuming that the solubility can be extrapolated at 550 $^{\circ}\text{C}$, it is equal

670 to $w_{Cr,ppm}^{Na} = 25 \cdot 10^{-3} \mu\text{g g}^{-1}$. Similarly, the solubilities at 550 $^{\circ}\text{C}$ of Mn [55], Fe [56], Ni [57] and Mo [1]

671 are 0.75, 0.52, 1.45 and 1.16 $\mu\text{g g}^{-1}$, respectively.

672 A rough mass balance was established for the first liquid sodium bath (section 2.3.1), taking into account

673 the solubility of the elements, the total area of the immersed samples (9 samples, 1.206 dm^2) and the

674 liquid sodium mass (2.3 kg). Assuming that all samples are dissolved in the same way, the maximum

675 total mass of dissolved steel per surface unit ($\Delta m_s^{(d)}$) can be estimated at $\Delta m_s^{(d)} = 8.3 \cdot 10^{-4} \text{ kg m}^{-2}$. When

676 immersed in liquid sodium, the steel samples dissolve and a layer of NaCrO_2 is formed. The mass gain

677 obtained between the initial sample and the sample taken out of the bath includes the formation of the

678 layer and the dissolution. Therefore, the mass gain due to formation of NaCrO_2 ($\Delta m_s^{(ox)}$) is given by:

679 $\Delta m_s^{(ox)} = \Delta m_s + \Delta m_s^{(d)} = 10.2 \pm 0.1 \cdot 10^{-4} \text{ kg m}^{-2}$ ($\Delta m_s = (1.9 \pm 0.1) \cdot 10^{-4} \text{ kg m}^{-2}$ for the first liquid

680 sodium bath only). This corresponds to a maximum oxide thickness of $230 \pm 10 \text{ nm}$ (Eq.4.1).

681 As a reminder, assuming that the decrease in Cr concentration of the steel is fully involved in the

682 formation of NaCrO_2 , the average thickness of this oxide would be 138 nm after 242 h of immersion

683 time and 670 nm after 3842 h (section 4.1.2). For the shortest corrosion times, the maximum oxide

684 thickness corresponding to Cr depletion is less than 230 nm. This means that the dissolution of the

685 elements is incomplete, i.e. the liquid sodium bath has not reached saturation. The NaCrO_2 layer can

686 therefore dissolve as it forms, as we have suggested in the reaction mechanisms above (section 4.1.3).

687 **4.2.2. Discussion on the solubility of the elements in the liquid sodium bath**

688 For long immersion times, the rough mass balance described above leads to a maximum oxide thickness

689 of 230 nm while the thickness estimated from Cr depletion reaches 670 nm. This means that the

690 dissolution of the elements estimated from the solubility of the pure elements is underestimated.

691 The measurements in the first liquid sodium bath are used here to estimate an order of magnitude of the

692 Cr solubility in sodium under our operating conditions. Nine samples were immersed in this sodium

693 bath, respectively for 242 , 584 , 1276 , 1924 , 2395 , 2830 , 3842 , 5304 and 7704 h. The change of

694 corrosion mechanisms occurs after about 4000 h (Fig. 1). Our interpretation is as follows: the sodium

695 bath is gradually enriched with Cr and reaches saturation after the first 4000 hours of our tests. The
696 solubility of Cr in liquid sodium containing $200 \mu\text{g}\cdot\text{g}^{-1}$ oxygen at 550°C can then be estimated from the
697 Cr profiles measured by GDOES for the samples immersed from 242 h to 3842 h (method presented in
698 Section 4.1.2). The amount of Cr released during the first 3842 h for samples immersed for 5304 and
699 7704 h cannot be measured. It is assumed to be equal to the amount of Cr released by the sample
700 immersed for 3842 h. Finally, the quantity of Cr released is then estimated at $2.09 \cdot 10^{-4}$ mol, or 10.9 mg.
701 The proportion used for oxide (considering a maximum thickness due to dissolution) is subtracted to
702 obtain the proportion of Cr released in the liquid sodium: $n_{Cr}^{Na} = 1.08 \cdot 10^{-4}$ mol, or 5.62 mg. For the first
703 test, the Cr concentration is then estimated at $w_{Cr,ppm}^{Na} = 2.44 \mu\text{g g}^{-1}$ at 3842 h (2.3 kg of liquid sodium).
704 This concentration is 98 times higher than the solubility of pure Cr in liquid sodium found in the
705 literature [54].

706 Such a high solubility of Cr in liquid sodium could result from the influence of other elements in
707 solution, such as Mn, Fe, Ni and Mo, which could increase the apparent solubility of Cr due to the
708 formation of intermetallic compounds. However, such compounds involving Cr have not yet been
709 reported in the literature to our knowledge. Another explanation could be the influence of oxygen on Cr
710 solubility that has already been observed [33,54] or the formation of a Na-Cr-O complex [25] but no
711 specific data were measured.

712 If this high value of Cr solubility in sodium is confirmed, its effects on corrosion modelling is of primary
713 importance. Indeed, the solubility is involved in the driving force of corrosion and only a small variation
714 of this parameter could lead to large changes in the corrosion modelling of steels [38] in liquid sodium
715 heat exchangers that could be used in future nuclear power plants. This new data shows the importance
716 of taking Cr selective oxidation into account when modelling corrosion.

717 With a longer immersion time ($t \geq 5304$ h), NaCrO_2 is characterized by XRD (Fig. 2) and the mass gain
718 of the samples increases significantly (Fig. 1). This change in behavior can be explained by the saturation
719 of liquid sodium with corrosion products containing chromium (Cr and NaCrO_2 or Na-Cr-O complex).

720 **4.3. Formation of M_6C and Na_4FeO_3**

721 In all tests, surface characterizations by XRD (Fig. 2) and SEM (Figs. 3 and 4), depth observations by
722 GDOES (Fig. 5) and STEM (Fig. 7) indicate the formation of M_6C carbides, where M is Mo and Fe.

723 Thermodynamic calculations confirmed the stability and composition of these carbides at 550 °C [33].
724 Since the surface of the steel is enriched with C when compared to the bulk, it can be concluded that the
725 carbon comes from liquid Na (carburization) [33]. The steel is slightly depleted in Mo under the
726 corrosion layer (depth > 1 μm in Fig. 5). This depletion is a sign of the formation of M₆C with the Mo
727 contained in the steel, although Mo may be present in liquid Na due to the dissolution of the crucible
728 (Mo structure).

729 More anecdotally, a particle containing O, Na and Fe is observed by TEM coupled to EDX (Fig. 8). This
730 particle could be Na₄FeO₃ which is the most stable compound containing Na, Fe and O [33,58] to our
731 knowledge. Thermodynamic calculations show that Na₄FeO₃ is stable in liquid sodium containing 200
732 μg g⁻¹ at a temperature below 350 °C [33,58]. This implies that Na₄FeO₃ was formed during the liquid
733 Na cooling step and not at 550°C. The observation of Na₄FeO₃ is unusual in our experiments (which
734 minimizes the impact of this artefact in our experimental protocol).

735 During immersion in liquid sodium, the mass of the samples increases through the formation of NaCrO₂
736 but also M₆C and Na₄FeO₃. However, the quantities of M₆C and Na₄FeO₃ formed are unknown and their
737 effects on mass gain cannot be calculated, although they are probably negligible. If a possible effect of
738 their formations were taken into account in our calculations, the calculated NaCrO₂ thickness would be
739 reduced, which would imply a higher unexplained amount of dissolved Cr, making no change in the
740 previous conclusions.

741

742 **5. Conclusions**

743 We studied the corrosion of 316L(N) stainless steel in static liquid sodium containing about $200 \mu\text{g g}^{-1}$
744 of oxygen at $550 \text{ }^\circ\text{C}$, for 239 h to 7704 h. Two additional specific tests were performed to locate the
745 oxidation reaction and measure the effect of transient temperature variations related to the handling of
746 samples. After the corrosion tests, the samples were characterized by techniques that provide
747 information on average corrosion behaviour, such as mass gain, XRD and GDOES. Local
748 characterizations were also performed such as EDX coupled to SEM on surfaces and cross sections,
749 STEM analysis of cross sections and SIMS analysis. These characterizations highlight reaction
750 mechanisms at the micrometric scale.

751 In our experiments, two different behaviors were identified as a function of immersion time in liquid
752 sodium, i.e. less than 3842 h or more than 5304 h. The transition was not precisely determined but falls
753 between these two experimental times examined.

754 First, for a time less than 3842 h, the samples have a low mass gain that remains constant over time. X-
755 ray diffraction only detects M_6C carbides where M is Mo and/or Fe and the austenitic matrix. The steel
756 surface is covered with tiny NaCrO_2 crystals that are too small to be detected by XRD but visible in the
757 Cr enrichment at the steel surface with GDOES. Steel is depleted in Cr, in the grains and in the vicinity
758 of the grain boundaries below the surface. The double-oxidation technique with ^{18}O and ^{16}O isotopes
759 coupled with a SIMS analysis revealed an oxygen enrichment in the grain boundaries of the steel at
760 depth. This means that the reaction interface for the NaCrO_2 formation is probably located at the
761 NaCrO_2 /steel interface and in the grain boundaries, which act as short circuits of diffusion.

762 For longer immersion times ($t \geq 5304 \text{ h}$), higher mass gains are measured corresponding to a thicker
763 sodium chromite layer, observed in cross section by SEM and detected by XRD. To explain these
764 experimental results, mass balances using the mass gain of each samples and the Cr depletion profiles
765 in the steel allowed us to propose reaction mechanisms for corrosion of the steel in liquid sodium: Cr
766 diffuses towards the surface of the steel and the O initially dissolved in the liquid sodium diffuses inside
767 the steel together with Na preferably through grain boundaries which are short diffusion circuits. They
768 react to form sodium chromite at the oxidation front located at the chromite/steel interface and in grain
769 boundaries. NaCrO_2 is formed for all immersion times but, at immersion times of less than 3842 h, a

770 significant difference (at least a factor of 100) between the amount of Cr present in the sodium chromite
771 actually observed on the samples and the amount of chromium leaving the metal estimated from the Cr
772 concentration profiles led to the conclusion that most of the chromium was dissolved in liquid sodium.
773 The increase in NaCrO₂ thickness at longer immersion times ($t \geq 5304$ h) is attributed to the saturation
774 of liquid sodium with corrosion products containing chromium (Cr and NaCrO₂ or Na-Cr-O complex)
775 in our experiments. The immersion time at which this phenomenon is observed is related to our
776 experimental protocol and cannot be extrapolated to other facilities. However, this shows the importance
777 of the solubility of Cr in liquid sodium for the corrosion of austenitic steels.

778 Our study shows that the Cr solubility in liquid sodium is underestimated by the pure Cr solubility law
779 found in the literature. One explanation could be that the solubility of Cr increases with the presence of
780 O dissolved by the formation of soluble sodium chromite or a Na-Cr-O complex. An order of magnitude
781 of the solubility of Cr evaluated with our experiments is $2.4 \mu\text{g g}^{-1}$ in liquid sodium containing $200 \mu\text{g}$
782 g^{-1} O at 550°C. The solubility of chromium could be the result of various contributions, pure Cr, NaCrO₂
783 and Na-Cr-O complex.

784 This new data shows the importance of taking Cr selective oxidation into account as well as its
785 dissolution mechanism for the long term modelling of stainless steel corrosion, as well as on the oxygen-
786 enhanced dissolution mechanism of iron.

787

788 **Acknowledgements**

789 The authors are extremely grateful to Jean-Bernard Guillot for fruitful discussions, to the CEA-
790 Generation 4 / Structural material project for part of the financial support, to V. Lorentz for the exposure
791 of the specimen to liquid sodium made in the Corrona-1 test Bench of the CEA-Saclay.

792 **Data availability**

793 The raw/processed data required to reproduce these findings cannot be shared at this time due to
794 technical or time limitations.

795

796 **6. References**

- 797 [1] H.U. Borgsted, C.K. Mathews, Applied chemistry of the alkali metals, Plenum Press, New-York,
798 1987, pp.183-184.
- 799 [2] F. Dalle, M. Blat-Yrieix, S. Dubiez-Le Goff, C. Cabet, P. Dubuisson, Conventional austenitic steels
800 as out-of-core materials for Generation IV nuclear reactors, in: Yvon, P. (Ed.), Structural Materials for
801 Generation IV Nuclear Reactors, Woodhead Publishing, 2017, pp. 595–633.
- 802 [3] M. Sarvghad, S.D. Maher, D. Collard, M. Tassan, G. Will, T.A. Steinberg, Materials compatibility
803 for the next generation of Concentrated Solar Power plants, Energy Storage Materials 14 (2018) 179-
804 198. <https://doi.org/10.1016/j.ensm.2018.02.023>.
- 805 [4] R. Dautray, Y. Bréchet, J. Friedel, Les fluides caloporteurs pour neutrons rapides, Académie des
806 sciences, EDPscience, Les Ulis, 2014.
- 807 [5] P.F. Tortorelli, Fundamentals of High-Temperature Corrosion in Liquid Metals, in: ASM Metals
808 Handbook, volume 13: Corrosion, 1987, pp. 112-121.
- 809 [6] T. Furukawa, S. Kato, E. Yoshida, Compatibility of FBR materials with sodium, J. Nucl. Mater. 392
810 (2009) 249-254.
- 811 [7] P. Baqué, A. Lafon, E. Sermet, L. Champeix, Contribution à l'étude de la corrosion de l'acier
812 austénitique bas carbone (AFNOR Z3 CN 18-10) par le sodium liquide à 700°C, J. Nucl. Mater. 54
813 (1974) 241-244.
- 814 [8] P. Baqué, L. Champeix, A. Lafon, E. Sermet, Some aspects of corrosion of austenitic steels in
815 flowing sodium, in: Liquid Alkali Metals, Proceedings of the International Conference Organized by
816 the British Nuclear Energy Society, Nottingham University, 1973, April 4-6, The British Nuclear Energy
817 Society, London, 1973, pp. 223-231.
- 818 [9] J.R. Weeks, H.S. Isaacs, Corrosion and deposition of steels and nickel-base alloys in liquid sodium,
819 in: Advances in corrosion science and technology, vol. 3, Plenum Press, New York, London, 1973, pp.
820 1-66.
- 821 [10] T. Suzuki, I. Mutoh, T. Yagi, Y. Ikenaga, Sodium corrosion behavior of austenitic alloys and
822 selective dissolution of chromium and nickel, J. Nucl. Mater. 139 (1986) 97-105.

823 [11] T. Gnanasekaran, R.K. Dayal, Liquid metal corrosion in nuclear reactor and accelerator driven
824 systems, in: D. Féron (Ed.), Nuclear Corrosion Science and Engineering, Woodhead Publishing Limited
825 – Cambridge, Philadelphia, 2012, pp.301-328.

826 [12] E. Yoshida, T. Furukawa, Corrosion issues in sodium-cooled fast reactor (SRF) systems, in: D.
827 Féron (Ed.), Nuclear Corrosion Science and Engineering, Woodhead Publishing Limited – Cambridge,
828 Philadelphia, 2012, pp.773-806.

829 [13] A.W. Thorley, C. Tyzack, Corrosion behaviour of steels and nickel alloys in high-temperature
830 sodium, in: Liquid Alkali Metals, proceeding of the International Conference organized by the British
831 Nuclear Energy Society, held at Nottingham University on 4-6 April 1973, London: London: The British
832 Nuclear Energy Society 1973, pp.257-273.

833 [14] B.H. Kolster, Mechanism of Fe and Cr transport by liquid sodium a non-isothermal loop system, J.
834 Nucl. Mater. 55 (1975) 155-168.

835 [15] J.L. Courouau, F. Masse, G. Rodriguez, C. Latge, B. Redon, The various sodium purification
836 techniques. International Working Group on Fast Reactors (IWGFR-98), IAEA: Vienna, 1997.

837 [16] L. Brissonneau, New considerations on the kinetics of mass transfer in sodium fast reactors: An
838 attempt to consider irradiation effects and low temperature corrosion, J. Nucl. Mater 423 (2012) 67-78.

839 [17] A.W. Thorley, J.A. Bardsley, Corrosion and mass transport of steel and nickel alloys in liquid
840 sodium system, in: Alkali Metal Coolants, Proceeding of the symposium, held by the International
841 Atomic Energy Agency in Vienna, 23 November – 2 December 1966, Vienna: International Atomic
842 Energy Agency 1967, pp.96-119.

843 [18] T. Suzuki, I. Mutoh, A revisit to “Steady state corrosion rate of type 316 stainless in liquid sodium
844 in a non-isothermal loop system”, J. Nucl. Mater. 165 (1989) 83.

845 [19] B.H. Kolster, The influence of sodium conditions on the rate for dissolution and metal oxygen
846 reaction of AISI 316 in liquid sodium, in: Second international conference on liquid metal technology
847 in energy production – Proceedings part 1, April 20-24, 1980, Richland, Washington, J.M. Dahlke 1980,
848 pp.7.53-7.61.

849 [20] M.V. Polley, G. Skyrme, An analysis of the corrosion of pure iron in sodium loop systems, J. Nucl.
850 Mater. 66 (1977) 221-235.

- 851 [21] J. Zhang, P. Hosemann, S. Maloy, Models of liquid metal corrosion, *J. Nucl. Mater* 404 (2010) 82-
852 96.
- 853 [22] B.A. Nevzorov, Corrosion of structural materials in sodium, Jerusalem: Israel program for scientific
854 translation 1970, translated from *Korroziya konstruktsionnykh materialov v natrii. Eksperimental'noe*
855 *issledovanie mekhanizma*, Moskva: Atomizdat 1968 (In Russian).
- 856 [23] R.M. Singer, A.H. Fleitman, J.R. Weeks, H.S. Isaacs, Measurement of the solubility of iron and
857 chromium in sodium, in: *Corrosion by liquid Metals, Proceedings of the sessions on corrosion by liquid*
858 *Metals of the 1969 fall meeting of the metallurgical society of AIME, October 13-16, 1969,*
859 *Philadelphia, Pennsylvania, New-york – London: Plenum Press 1970, pp.561-576.*
- 860 [24] W.P. Stanaway, R. Thompson, Solubility of metals, iron and manganese in sodium, in: *Second*
861 *international conference on liquid metal technology in energy production – Proceeding part 2, April 20-*
862 *24, 1980, Richland, Washington, J.M. Dahlke 1980, pp.421-427.*
- 863 [25] B.H. Kolster, L. Bos, Sodium corrosion in a total molybdenum loop system: construction,
864 experience and results, in: *Liquid metal engineering and technology, London: The British Nuclear*
865 *Energy Society 1984, pp.235-242.*
- 866 [26] T. Gnanasekaran, C.K. Mathews, Threshold oxygen levels in sodium necessary for the formation
867 of NaCrO_2 in sodium-steel systems, *J. Nucl. Mater.* 140 (1986) 202-213.
- 868 [27] A.G. Crouch, P.R. Bussey, Corrosion of ferritic steels in flowing sodium, in: *Ferritic steels for fast*
869 *reactor steam generators, London: The British Nuclear Energy Society 1978, pp.258-263.*
- 870 [28] A.W. Thorley J.A. Bardsley, Structural changes in materials exposed to liquid sodium, *J. R.*
871 *Microsc. Soc.* 88-4 (1968) 431-447.
- 872 [29] A.G. Crouch, The growth and stability of sodium chromite and its influence on corrosion, in:
873 *Second international conference on liquid metal technology in energy production – Proceedings part 1,*
874 *April 20-24, 1980, Richland, Washington, J.M. Dahlke 1980, pp. 3.43-3.51.*
- 875 [30] I.W. Cavell, M.G. Nicholas, Some observations concerned with the formation of sodium chromite
876 on AISI 316 exposed to oxygenated sodium, *J. Nucl. Mater.* 95 (1980) 129-144.
- 877 [31] I.W. Cavell, M.G. Nicholas, Study of the formation of sodium chromite on some ferrous alloys and
878 chromium plate exposed to oxygenated sodium, *J. Nucl. Mater.* 95 (1980) 145-154.

879 [32] P.L.F. Rademakers, B.H. Kolster, Corrosion of various ferritic steels in an isothermal sodium loop
880 system, *J. Nucl. Mater* 97 (1981) 309-318.

881 [33] M. Rivollier, J.-L. Courouau, M. Tabarant, C. Blanc, M.-L. Giorgi, Oxidation of 316L(N) Stainless
882 Steel in Liquid sodium at 650 °C, *J. Nucl. Mater.* 500 (2018) 337-348.
883 <https://doi.org/10.1016/j.jnucmat.2017.12.037>.

884 [34] J.H. Kim, S.H. Kim, Microstructure and mechanical property of ferritic-martensitic steel cladding
885 under a 650 °C liquid sodium environment, *J. Nucl. Mater.* 443 (2013) 112-119.

886 [35] S.H. Shin, J. Lee, J.H. Kim, J.H. Kim, Mechanism of corrosion of 9Cr and 12 Cr ferritic/martensitic
887 steels under oxygen-saturated sodium, *Corros. Sci.* 112 (2016) 611-624.

888 [36] S.H. Shin, J.H. Kim, J.H. Kim, Corrosion behaviour and microstructural evolution of ASTM A182
889 Grade 92 steel in liquid sodium at 650 °C, *Corros. Sci.* 97 (2015) 172-182.

890 [37] E.L. Zebroski, R.S. Young, F.A. Comprelli, Effects of mass transfer, and of changes in properties,
891 on austenitic steels in flowing sodium, in: *Alkali Metal Coolant, Proceedings of a symposium, Vienne:*
892 *IAEA, 1967, pp.195-211.*

893 [38] S. Ohtsuka, T. Tanno, H. Oka, Y. Yano, S. Kato, T. Furukawa, T. Kaito, Model calculation of Cr
894 dissolution behavior of ODS ferritic steel in liquid high-temperature flowing sodium environment, *J.*
895 *Nucl. Mater.* 505 (2018) 44-53. <https://doi.org/10.2016/J.nucmat.2018.03.054>.

896 [39] J.L. Courouau, F. Balbaud-Célérier, V. Lorentz, T. Dufrenoy, Corrosion by liquid sodium of
897 materials for sodium fast reactors: the CORRONa testing device, in: *the proceedings of the International*
898 *Congress on Advances in Nuclear Power Plants (ICAPP '11), paper 11152, Nice, France, May 2-5, 2011.*

899 [40] J.-L. Courouau, M.-C. Steil, J. Fouletier, F. Rouillard, V. Lorentz, P. Bonnaillie, A. Muccioli, J.
900 Unger, S. Tricoit, M. Tabarant, Single Crystal and Sintered Alumina Corrosion in Liquid Sodium. *Oxid.*
901 *Met.* 87 (2017), 789–800. <https://doi.org/10.1007/s11085-017-9743-3>.

902 [41] Rouillard, F., Courouau, J.-L., Duprey, B., Mathieu, S., Vilasi, M., Bouizi, Y., Boissonnet, G.,
903 Pedraza, F., Proriol-Serre, I., 2017. Evaluation of the Compatibility of Aluminide Coatings in High-
904 Temperature Sodium for Fast Reactor Application. *Oxid. Met.* 88 (2017), 221–233.
905 <https://doi.org/10.1007/s11085-016-9689-x>.

906 [42] S.N. Basu, J.W. Halloran, Tracer isotope distribution in growing oxide scales, *Oxid. Met.* 27 (1987)
907 143-155.

908 [43] J. Jedlinski, G. Borchardt, On the oxidation mechanism of alumina formers, *Oxid. Met.* 36 (1991)
909 317-337.

910 [44] S. Chevalier, G. Strehl, J. Favergeon, F. Desserey, S. Weber, O. Heintz, G. Borchardt, J.P. Larpin,
911 Use of oxygen isotope to study the transport mechanism during high temperature oxide scale growth,
912 *Mater. high temp.* 20 (2003) 253-259.

913 [45] J. Philibert, *Diffusion and Mass Transport in Solids*, Éditions de Physique, Les Ulis, 1991.

914 [46] M. Auinger, V. G. Praig, B. Linder, H. Danninger, Grain boundary oxidation in iron-based alloys,
915 investigated by ¹⁸O enriched water vapour – The effect of mixed oxides in binary and ternary Fe-{Al,
916 Cr, Mn, Si} systems, *Corros. Sci.* 96 (2015) 133-143.

917 [47] L.G. Harrison, Influence of dislocations on diffusion kinetics in solid with particular reference to
918 the alkali halides, *Trans. Faraday Soc.* 57 (1961) 1191-1199.

919 [48] H. Mehrer, *Diffusion in solid*, *Solid State Science* 155, ed. M Cardona *et al.*, Springer, Berlin, 2007.

920 [49] J.C. Fisher, Calculation of Diffusion Penetration Curves for Surface and Grain boundary Diffusion,
921 *J. Appl. Phys.* 22-1 (1951) 74-77.

922 [50] J. Crank, *The mathematics of diffusion*, Oxford University Press, Oxford, 1975.

923 [51] A.D. Le Claire, The analysis of grain boundary diffusion measurements, *British Journal of Applied*
924 *Physics* 14 (1963), 351-366.

925 [52] I. Kaur, Y. Mishin, W. Gust, *Fundamentals of grain and interphase boundary diffusion*, Wiley,
926 Chichester, 1995.

927 [53] J.D. Noden, A general equation for the solubility of oxygen in liquid sodium – addendum, *J. Br.*
928 *Nucl. Energy* 12-1 (1973) 329-331.

929 [54] R.M. Singer, A.H. Fleitman, J.R. Weeks, H.S. Isaacs, Measurements of the solubility of iron and
930 chromium in sodium, in: J.E. Draley, J.R. Weeks (EDS), *Corrosion by liquid metals*, Plenum Press,
931 New-York, 1970, pp. 561-576.

932 [55] W.P. Stanaway, R. Thompson, The solubility of transition metals, Mn and Co in liquid sodium, in:
933 H.U. Borgstedt (Eds), Material behavior and physical chemistry in liquid metal system, Plenum Press,
934 New York – London, 1982, pp. 421-427.

935 [56] W.P. Stanaway et R. Thompson, Solubility of metals, iron and manganese in sodium, in: J.M.
936 Dahlke (Eds), Second international conference on liquid metal technology in energy production,
937 American Nuclear Society Materials Science and Technology Division, Richland, 1980, pp. 18-54 – 18-
938 61.

939 [57] S.P. Awasthi, H.U. Borgstedt, An assessment of solubility of some transition metals (Fe, Ni, Mn
940 and Cr) in liquid sodium, J. Nucl. Mater. 116 (1983) 103-111.

941 [58] B.J. Shaiu, P.C.S. Wu, P. Chiotti, Thermodynamic properties of the double oxide of Na₂O with the
942 oxides of Cr, Ni and Fe, J. Nucl. Mater. 67 (1977) 13-23.

943

944 **Table 1.** Composition in wt.% of stainless steel 316L(N) tested.

945 **Figure 1.** Mass evolution as a function of immersion time of 316L(N) stainless steel in liquid sodium
946 containing $200 \mu\text{g g}^{-1}$ of oxygen at $550 \text{ }^\circ\text{C}$ (first Na bath: \diamond , second Na bath: \bullet compared to \otimes where
947 the samples were immersed and removed at $550 \text{ }^\circ\text{C}$, third Na bath: \times). The mass gain of the steel samples
948 increases significantly after 4000 h of corrosion.

949 **Figure 2.** XRD diffraction patterns of 316L(N) steel immersed for 1460 h (bottom dark line) and 5304
950 h (top blue line) in liquid sodium containing $200 \mu\text{g g}^{-1}$ of oxygen at $550 \text{ }^\circ\text{C}$, compared with the
951 diffraction patterns of NaCrO_2 , austenite and $\text{Fe}_3\text{Mo}_3\text{C}$.

952 **Figure 3.** SEM observations of 316L(N) specimen immersed during 1460 h in liquid sodium containing
953 $200 \mu\text{g g}^{-1}$ of oxygen at $550 \text{ }^\circ\text{C}$ (back-scattered electron mode). The steel surface is covered with dark
954 grey and white particles. The surface density of the dark grey particles varies from place to place,
955 possibly in relation to the orientation of the underlying austenite grains.

956 **Figure 4.** EDX elementary maps of the sample immersed during 1460 h in liquid sodium containing
957 $200 \mu\text{g g}^{-1}$ of oxygen. The steel surface is covered with small particles rich in O, Na and Cr and larger
958 particles rich in Mo.

959 **Figure 5.** Elementary composition profile measured by GDOES from the steel surface to a depth of 5
960 μm for a 316L(N) specimen immersed during 1460 h in liquid sodium containing $200 \mu\text{g g}^{-1}$ of oxygen
961 at $550 \text{ }^\circ\text{C}$: C (thin black line), O (light grey line), Na (grey line), Cr (dotted line), Mn (dark grey line),
962 Fe (thick black line), Ni (dashed line) and Mo (double thin line). The red dotted vertical line delimits
963 the oxide layer rich in O, Na and Cr.

964 **Figure 6.** Chromium concentration profiles obtained by GDOES, after 500, 1000 and 1460 h of
965 immersion in liquid sodium at $550 \text{ }^\circ\text{C}$ containing $200 \mu\text{g g}^{-1}$ of oxygen, the measurement uncertainties
966 are calculated using at least two GDOES profiles.

967 **Figure 7.** HAADF images of a cross section of a sample immersed for 1460 h at $550 \text{ }^\circ\text{C}$ in liquid sodium
968 with $200 \mu\text{g g}^{-1}$ of oxygen. The sample surface is covered with a layer composed of two types of particles
969 (dark and light in appearance) and the grain boundary also contains different types of particles up to a
970 distance of $2 \mu\text{m}$.

971 **Figure 8.** EDX elementary mapping of a cross section of a sample immersed during 1460 h in liquid
972 sodium containing $200 \mu\text{g g}^{-1}$ of oxygen (enlarged view of Fig. 7). Some particles are rich in O, Na and
973 Cr (probably corresponding to NaCrO_2) and others are rich in Fe and Mo (probably corresponding to
974 M_6C carbides).

975 **Figure 9.** Chromium EDX profiles along the grain boundary from the sample surface (profiles 1 to 4
976 shown by arrows in Fig. 7), specimen immersed during 1460 h in liquid sodium containing $200 \mu\text{g g}^{-1}$
977 of oxygen at 550°C . Cr depletion is observed in the grain boundary and in the grains. This Cr depletion
978 decreases from the sample surface to the bulk. Cr profiles are also observed to be asymmetric.

979 **Figure 10.** Cartographies of ^{18}O (top) and ^{16}O (bottom) at several surface depths for a sample immersed
980 for 1460 h in liquid sodium containing $200 \mu\text{g g}^{-1}$ of oxygen at 550°C . At $1.4 \mu\text{m}$ depth, oxygen is
981 located mainly at grain boundaries and ^{18}O appears to be more present than ^{16}O .

982 **Figure 11.** ^{16}O and ^{18}O concentration profiles obtained by SIMS in the grains (left column, Fig. 11a,
983 11c and 11e) and at the grain boundaries (right column, Fig. 11b, 11d and 11f) for 600 h (Fig. 11a and
984 11b), 1000 h (Fig. 11c and 11d) and 1460 h (Fig. 11e and 11f). The oxygen profiles are compared with
985 the ^{16}O profile obtained in the first corrosion step (500 h in ^{16}O containing liquid sodium black dotted
986 line). The example chosen is corrosion in liquid sodium at 550°C containing $200 \mu\text{g g}^{-1}$ of oxygen. For
987 each corrosion time, the oxygen (^{16}O and ^{18}O) concentration and oxidation depth are higher in the grain
988 boundaries than in the grains. The ^{18}O concentration increases with corrosion time both in the grains and
989 at the grain boundaries.

990 **Figure 12.** Relative abundance profiles of ^{18}O obtained by SIMS, from the sample surface along the
991 grains (a) and grain boundaries (b) for samples immersed in liquid sodium at 550°C containing $200 \mu\text{g}$
992 g^{-1} of oxygen. Fast oxygen diffusion along the austenite grain boundaries is clearly visible throughout
993 the immersion period.

994 **Figure 13.** Cross section of a sample immersed for 7704 h in liquid sodium containing $200 \mu\text{g g}^{-1}$ of
995 oxygen at 550°C . (a) secondary electron image, (b), (c), (d), (e) and (f) EDX mapping for, respectively
996 oxygen, sodium, chromium, iron and molybdenum.

997

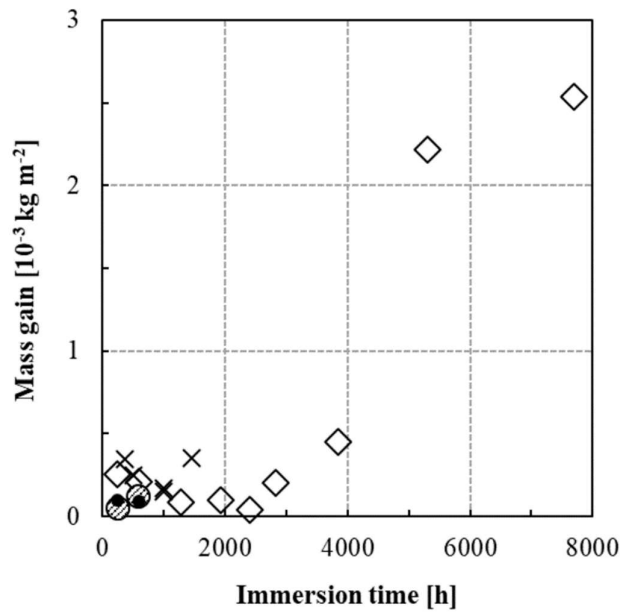
998 Table 1. Composition in wt.% of stainless steel 316L(N) tested.

Fe	Cr	Ni	Mo	Mn	C	Si	Ti	Al	Cu	Co
Balanced	17.9	12.1	2.35	1.72	0.012	0.45	0.0015	0.0025	0.0025	0.0008

999

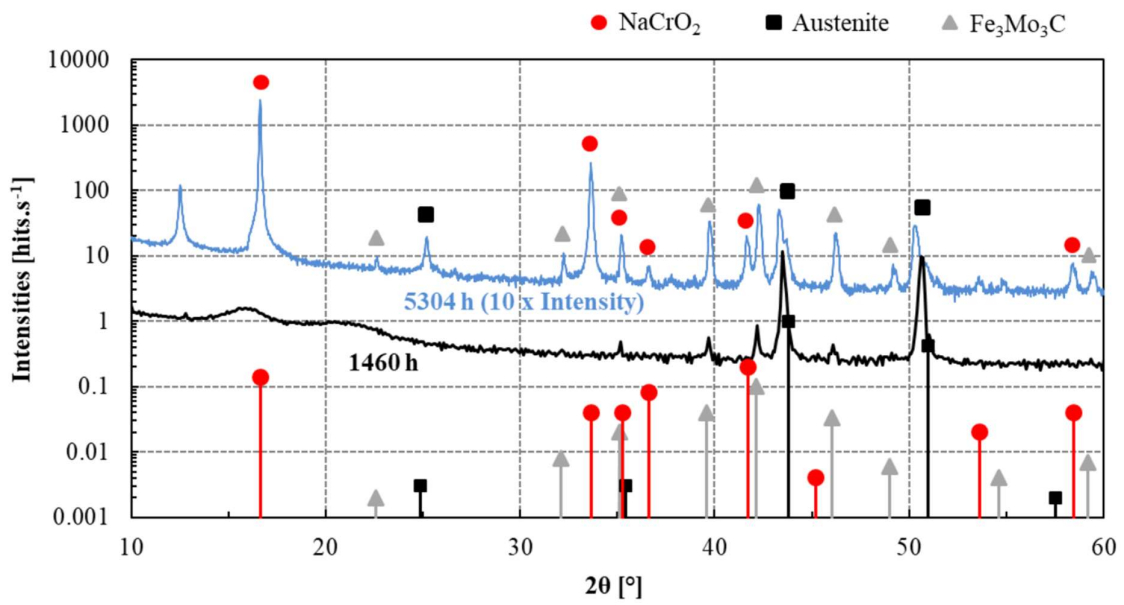
1000

1001 Figure 1.



1002

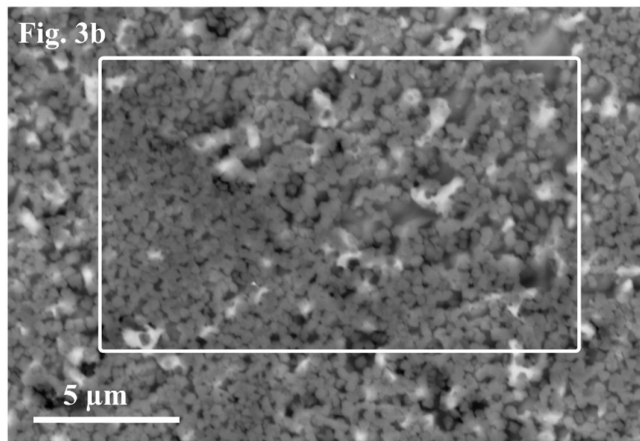
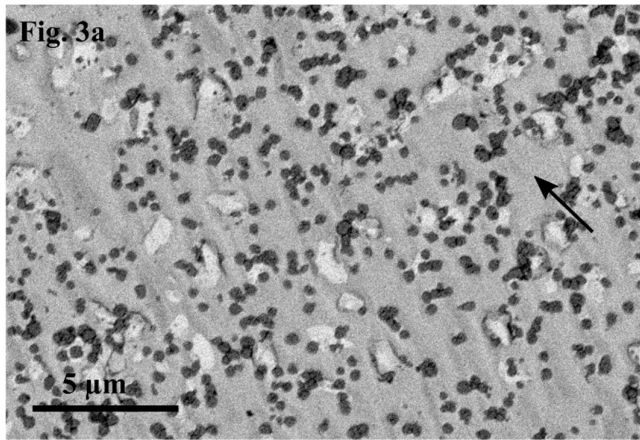
1003 Figure 2.



1004

1005

1006 Figure 3.



1007

1008

1009 Figure 4.

Fig. 4a. Oxygen

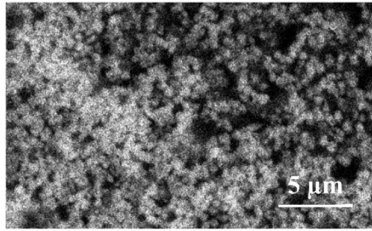


Fig. 4b. Sodium

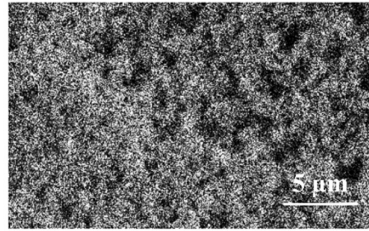


Fig. 4c. Chromium

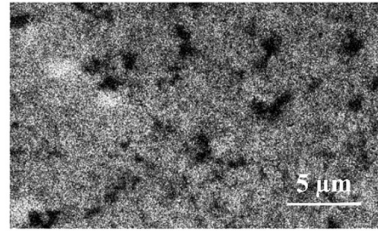


Fig. 4d. Iron

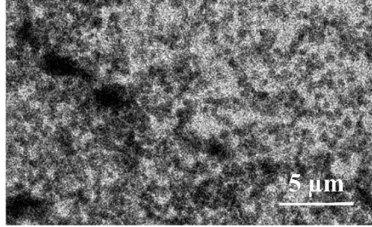


Fig. 4e. Nickel

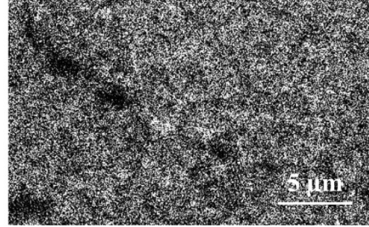
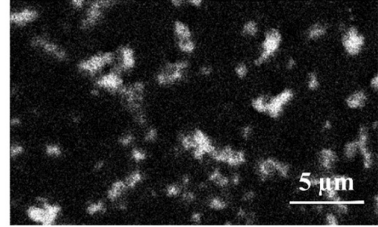


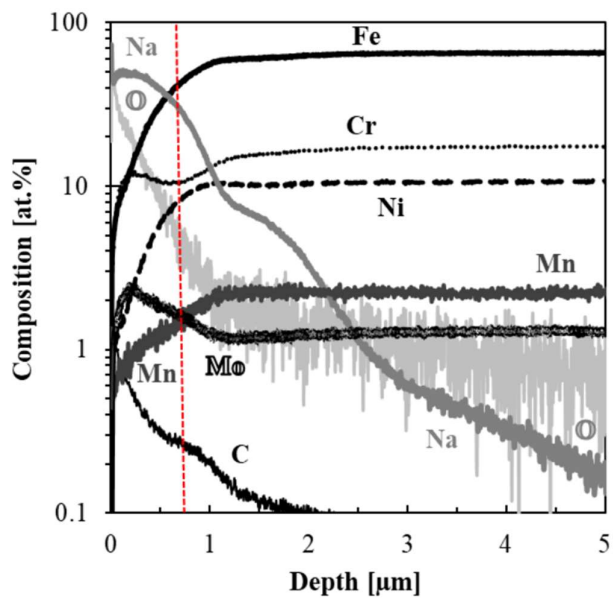
Fig. 4f. Molybdenum



1010

1011

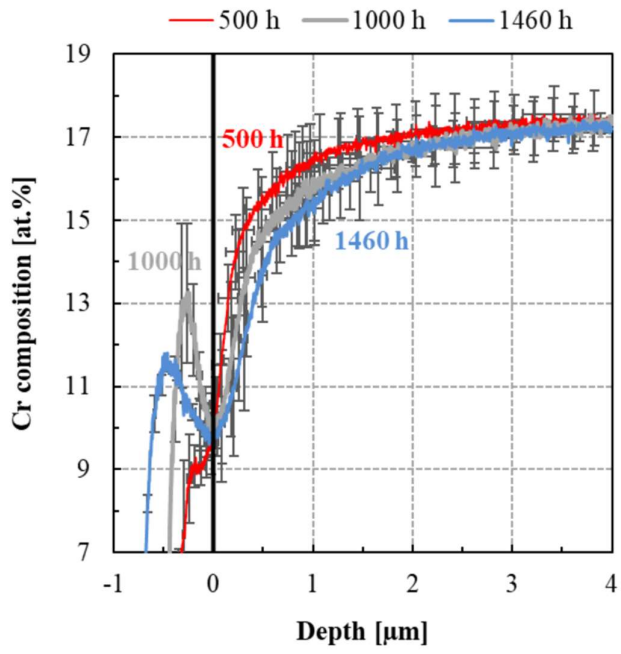
1012 Figure 5.



1013

1014

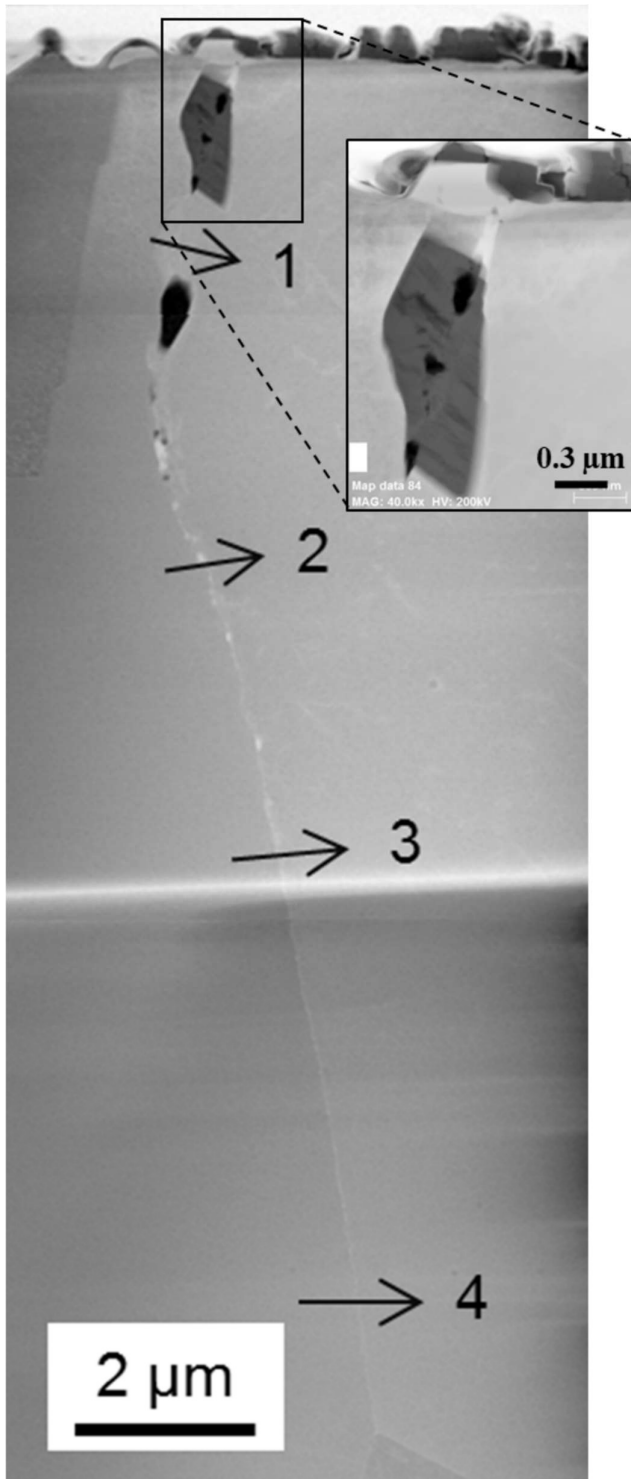
1015 Figure 6.



1016

1017

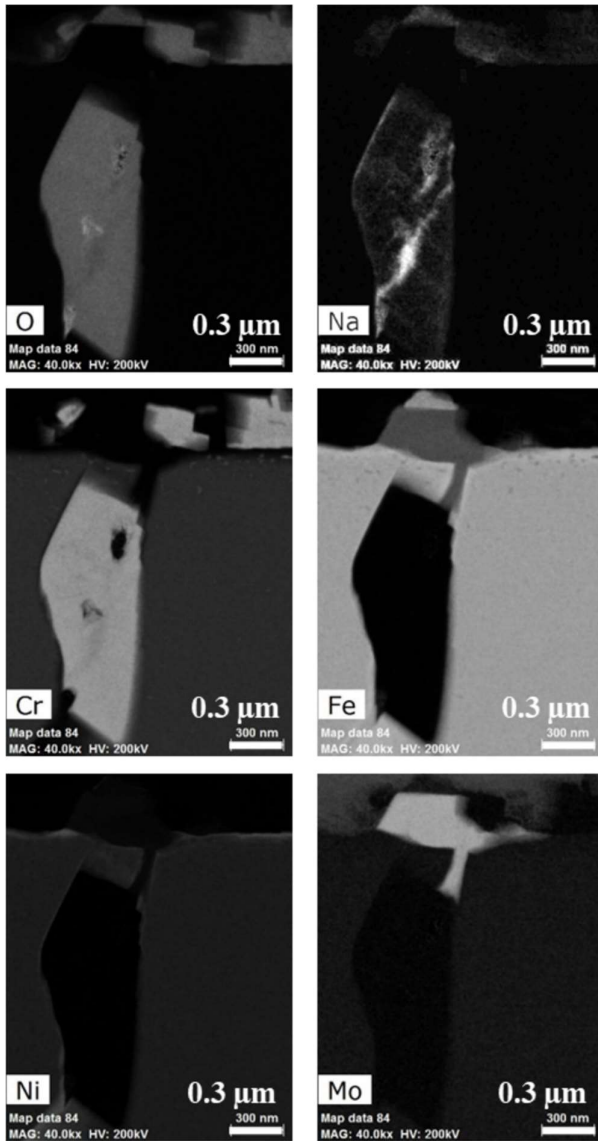
1018 Figure 7.



1019

1020

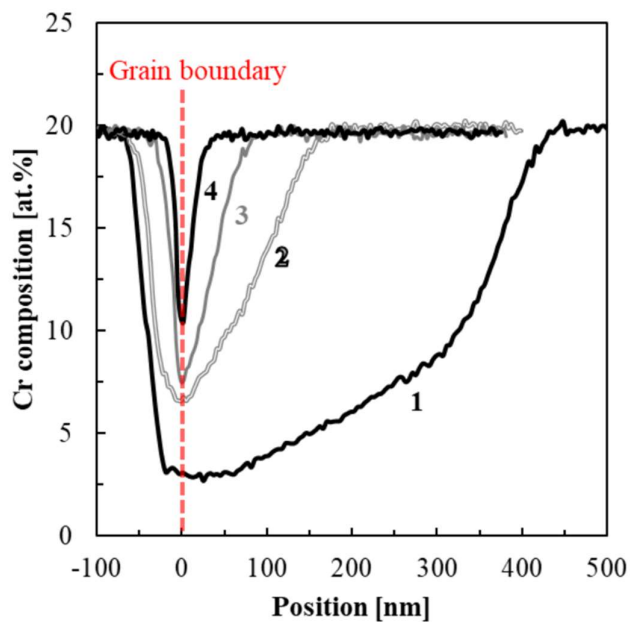
1021 Figure 8.



1022

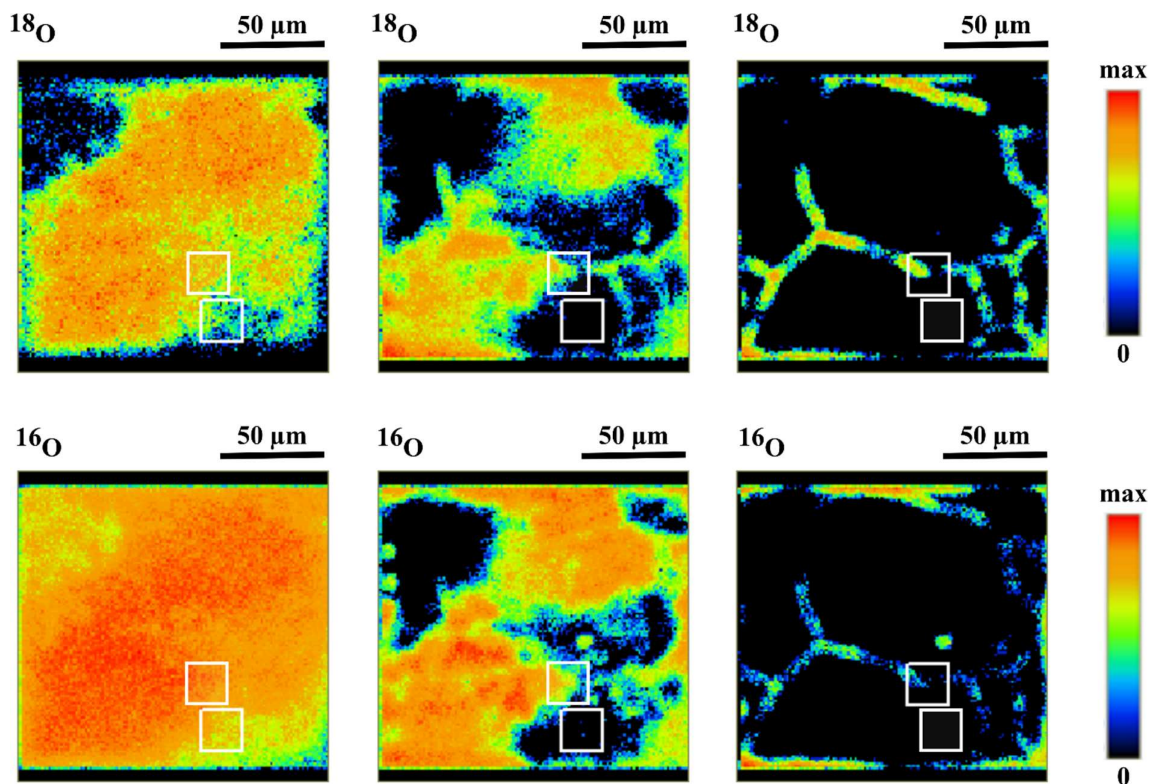
1023

1024 Figure 9.



1025

1026 Figure 10.



1027

1028

1029 Sputtered depth from the interface

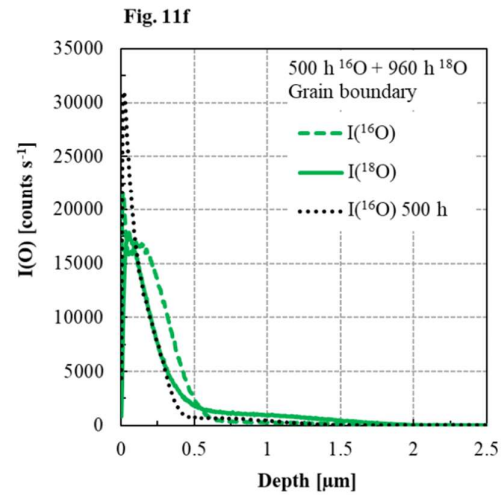
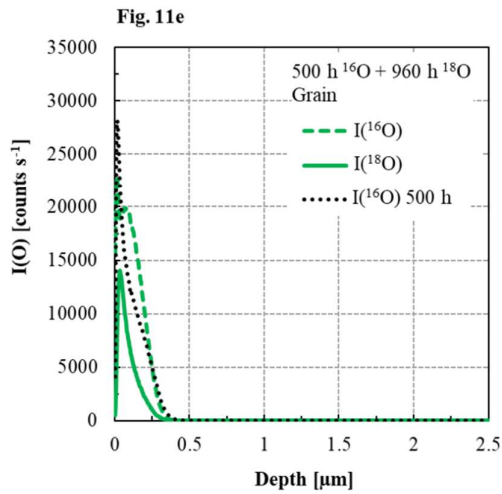
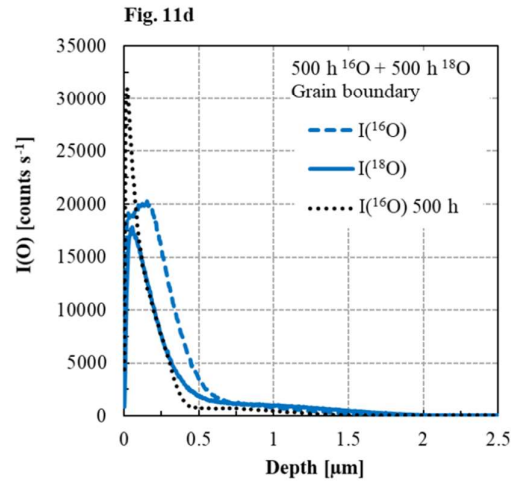
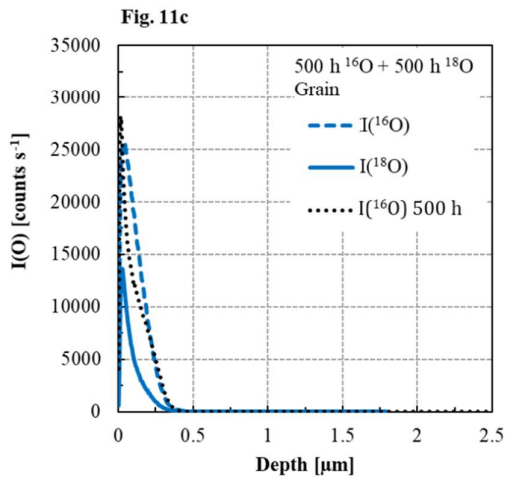
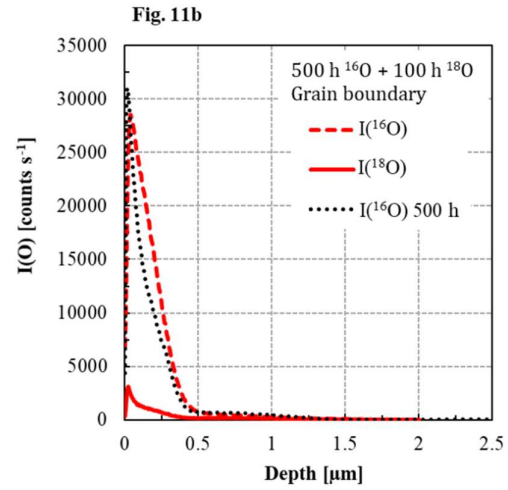
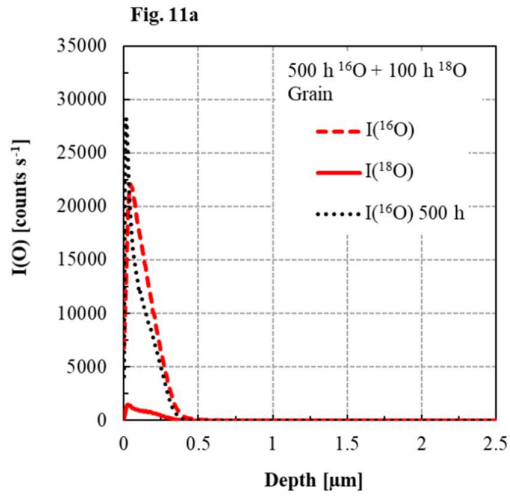
1030 $0.02 \pm 0.01 \mu\text{m}$

1031

$0.6 \pm 0.03 \mu\text{m}$

$1.4 \pm 0.5 \mu\text{m}$

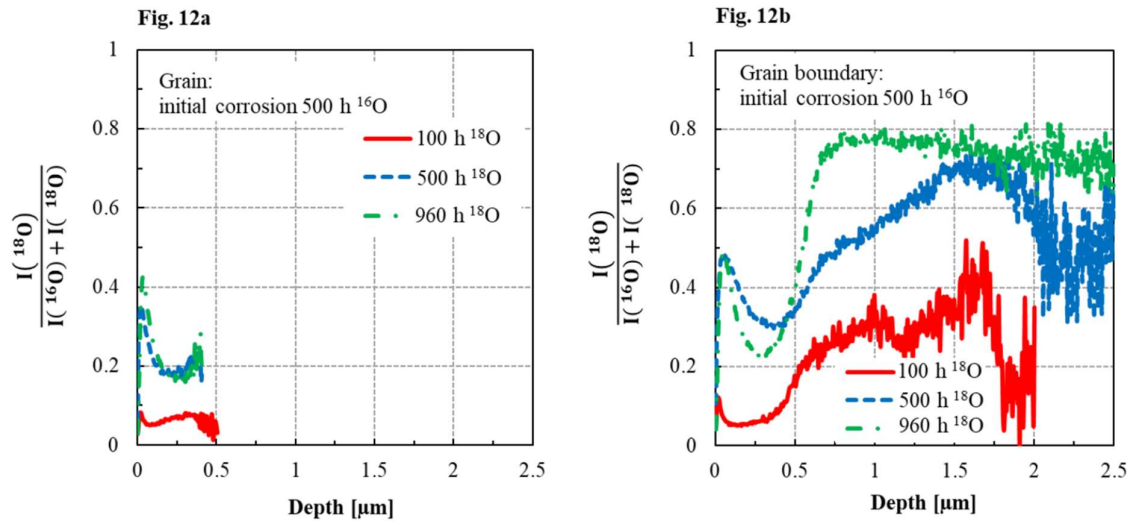
1032 Figure 11.



1033

1034

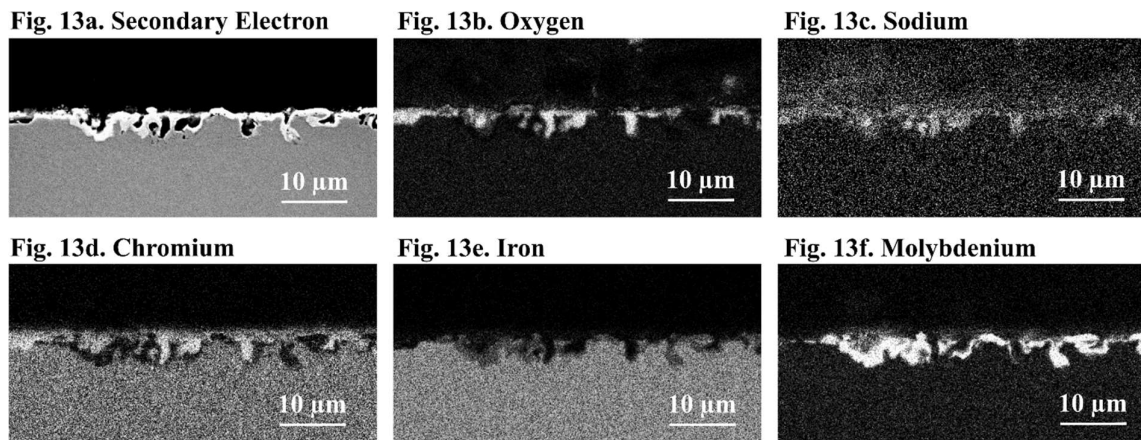
1035 Figure 12.



1036

1037

1038 Figure 13.



1039

1040